12-17-2015

Oscillatory Network Dynamics in Perceptual Decision-Making

Ganesh Chand

Recommended Citation
Chand, Ganesh, "Oscillatory Network Dynamics in Perceptual Decision-Making." Dissertation, Georgia State University, 2015.
doi: https://doi.org/10.57709/7885579

OSCILLATORY NETWORK DYNAMICS IN PERCEPTUAL DECISION-MAKING

By

GANESH CHAND

Under the Direction of Mukesh Dhamala, PhD

ABSTRACT

Synchronized oscillations of ensembles of neurons in the brain underlie human cognition and behaviors. Neuronal network oscillations can be described by the physics of coupled dynamical systems. This dissertation examines the dynamic network activities in two distinct neurocognitive networks, the salience network (SN) and the ventral temporal cortex-dorsolateral prefrontal cortex (VTC-DLPFC) network, during perceptual decision-making (PDM).

The key nodes of the SN include the right anterior insula (rAI), left anterior insula (lAI), and dorsal anterior cingulate cortex (dACC) in the brain. When and how a sensory signal enters and organizes within the SN before reaching the central executive network including the prefrontal cortex has been a mystery. Second, prior studies also report that perception of visual objects (face and house) involves a network of the VTC—the fusiform face area (FFA) and para-hippocampal place area (PPA)—and the DLPFC. How sensory information enters and organizes

within the VTC-DLPFC network is not well understood, in milliseconds time-scale of human's perception and decision-making. We used clear and noisy face/house image categorization tasks and scalp electroencephalography (EEG) recordings to study the dynamics of these networks. We demonstrated that beta (13–30 Hz) oscillation bound the SN, became most active around 100 ms after the stimulus onset, the rAI acted as a main outflow hub within the SN, and the SN activities were negatively correlated with the difficult tasks. We also uncovered that the VTC-DLPFC network activities were mediated by beta (13-30 Hz) and gamma (30-100 Hz) oscillations. Beta activities were enhanced in the time frame 125-250 ms after stimulus onset, the VTC acted as main outflow hub, and network activities were negatively correlated with the difficult tasks. In contrast, gamma activities were elevated in the time frame 0-125 ms, the DLPFC acted as a main outflow hub, and network activities—specifically the FFA-PPA pair—were positively correlated with the difficult tasks. These findings significantly enhance our understanding of how sensory information enters and organizes within the SN and the VTC-DLPFC network, respectively in PDM.

INDEX WORDS: Electroencephalography (EEG), Neuronal oscillations, Perceptual decision-making, Salience network (SN), Fusiform face area (FFA), Parahippocampal place area (PPA), Dorsolateral prefrontal cortex (DLPFC)

OSCILLATORY NETWORK DYNAMICS IN PERCEPTUAL DECISION-MAKING

by

GANESH CHAND

A Dissertation Submitted in Partial Fulfillment of the Requirements for the Degree of

Doctor of Philosophy

in the College of Arts and Sciences

Georgia State University

2015

OSCILLATORY NETWORK DYNAMICS IN PERCEPTUAL DECISION-MAKING

by

GANESH CHAND

Committee Chair: Mukesh Dhamala

Committee: Vadym Apalkov

Brian Thoms

Unil Perera

Yohannes Abate

Misty Bentz

Electronic Version Approved:

Office of Graduate Studies

College of Arts and Sciences

Georgia State University

December 2015

DEDICATION

I would like to dedicate this dissertation to my parents, wife, daughter, and sister for their unconditional love, patience, and support.

ACKNOWLEDGEMENTS

I am deeply indebted to many wonderful people who have supported me to come up with this dissertation. My foremost sincere thanks go to my PhD supervisor Dr. Mukesh Dhamala, who provided me enormous opportunities in the research field of my interest. He motivated me and put in a lot of effort and his invaluable expertise being available for extensive discussions. He guided, encouraged, and inspired to aim high in my goals throughout my PhD.

I am thankful to all wonderful colleagues of Dr. Dhamala's Neurophysics laboratory, with whom I spent great time, had fun, and extensively discussed research problems during my PhD period. My special thanks go to the members of my dissertation committee. I am thankful to previous chair Dr. H. Richard Miller and present chair Dr. D. Michael Crenshaw, Department of Physics and Astronomy, for providing me their valuable time and supports when I needed. I would also like to extend my thanks to previous graduate program director Dr. A. G. Unil Perera and present graduate program director Dr. Xiaochun He for providing me their supports and guidance to complete courses.

I would especially like to thank all participants who took part in my studies. Finally, I would like to thank all my family members, relatives and friends for their love and supports.

TABLE OF CONTENTS

LIST OF TABLES

LIST OF FIGURES

LIST OF ACRONYMS

ANOVA	Analysis of variance
BA	Brodmann area
BESA	Brain electrical source analysis
BOLD	Blood oxygen level dependent
CEN	Central executive network
dACC	Dorsal anterior cingulate cortex
DLPFC	Dorsolateral prefrontal cortex
DMN	Default mode network
DTI	Diffusion tensor imaging
EEG	Electroencephalography
ERPs	Event related potentials
FDR	False discovery rate
FFA	Fusiform face area
FFT	Fast Fourier transforms
fMRI	Functional magnetic resonance imaging
GC	Granger causality
Hz	Hertz
iFFT	Inverse fast Fourier transforms
ICA	Independent component analysis
lAI	Left anterior insula
LORETA	Low resolution electromagnetic tomography

MEG	Magnetoencephalography
MNI	Montreal neurological institute
ms	Milliseconds
PDM	Perceptual decision-making
PPA	Para-hippocampal place area
rAI	Right anterior insula
RT	Response time
SN	Salience network
TF	Time frame
VTC	Ventral temporal cortex
0% (noise)	Stimuli with 0% noise added
40% (noise)	Stimuli with 40% noise added
55% (noise)	Stimuli with 55% noise added

1 INTRODUCTION

1.1 Overview

Our everyday lives involve making decisions. Whenever there are two or more alternatives, one can decide between them. This seems very simple, but as a neurophysicist, an obvious wonderment is how the brain carries out this decision. What brain areas are involved? How do they coordinate to arrive at a perceptual decision? These are some of the questions, answers of which can take us closer to solving mysteries of brain decision-making functions.

The human brain is a highly complex system consisting of a large number of interconnected nerve cells (neurons) carrying out perception, cognition and action. Those neuronal connections enable various brain structures to exchange information with each other during a perceptual or cognitive task. How neuronal systems interact in cognitive tasks including decision-making is not completely uncovered. Perceptual decision-making (PDM) is a process of decision-making based on available sensory information and evidence. Prior investigation proposes the PDM as an encoding of sensory evidence, planning of actions, and mapping of sensory information into action plans (1). Such a sensory information-guided, goal-directed behavior is thought to entail the flexible interactions among task-relevant, but widely distributed brain areas (2, 3). However, ‘where in the brain’, ‘when in the brain’ and ‘how in the brain’ questions are not well answered. In other words, how sensory signal enters and organizes within those brain areas before motor-execution are largely unknown. Such understanding is crucial not only for basic research questions but also for creating a pipeline to treat the patients who have impaired decision-making. My PhD research projects seek to uncover those mysteries in the

human brain during PDM processes. The findings of my PhD work have been reported in the following first author peer-reviewed journal papers.

1. **Chand GB** and Dhamala M. The salience network dynamics in perceptual decision-making. NeuroImage (Under Revision).

2. **Chand GB**, Lamichhane B and Dhamala M. Face or house image perception: beta and gamma bands of oscillations in brain networks carry out the decision. Brain Connectivity (Under Revision).

3. **Chand GB** and Dhamala M. Interactions among the default-mode, salience and central-executive networks during perceptual decision-making of moving dots. Brain Connectivity (Under Revision).

4. **Chand GB** and Dhamala M. Oscillatory causal interactions between the salience and central-executive networks during perceptual decision-making. NeuroImage (Under Revision).

5. **Chand GB** and Dhamala M. Spectral factorization-based current source density analysis of ongoing neural oscillations. Journal of Neuroscience Methods 224, 58-65 (2014).

In the first paper, I investigate the salience network dynamics for the first time in finer time-scale (milliseconds). In the second paper, I demonstrate for the first time that the band-specific oscillatory networks features and their temporal dynamics in visual perception. In the third paper, I apply a unified network approach to examine the interactions among the default-mode, salience and central-executive networks during easier versus harder PDM tasks. The fourth paper demonstrates band-specific temporal features between the salience network and central-executive network in PDM. The fifth paper (4) is about the technique, where I propose an algorithm that localize neuronal oscillations, especially ongoing/spontaneous oscillations. Except my fifth paper, all of the journal papers aim to unravel the underlying brain mechanisms

involved in PDM. Here, I include only the first two peer-reviewed journal papers in this dissertation.

1.2 Neuronal oscillations and synchrony

The human brain consists of billions of neurons—the cells that transmit information inside the brain—and each of which have more than 10^3 synaptic connections which enable neuronal assembles to oscillate and synchronize transiently or connect functionally (5). Neuronal oscillations can be captured at various measurement scales: at a single neuron level, at local field potentials level, and at large-scales level (5, 6). Scalp electroencephalography (EEG) is a noninvasive electrophysiological recording technique that measures synchronized activity of ensembles of neurons (7). Hans Berger was the first one to record a version of EEG from the human in 1924 (8). Since then EEG has become a valuable tool for the study of brain functions and dysfunctions (7, 9, 10).

EEG is relatively convenient to demonstrate the physiological manifestations of synchronized activity in a time-scale (i.e., milliseconds) of the human sensory perception and decision-making. EEG signals captured from the brain comprise a broad range of synchronized oscillatory activities, which are tentatively categorized into several bands: delta (1-4 Hz), theta (4-8 Hz), alpha (8-13 Hz), beta (13-30 Hz), and gamma (30–100 Hz) (11). These oscillatory contents subserve important functions in the brain (12-14). However, an important but unsolved question is whether these bands exhibit distinct physiological roles and whether specific sensorimotor, perceptual or cognitive operations are tied to them (11, 14). Some of these oscillations are illustrated to be a physiological signature of different cognitive states (15, 16) with or without tasks. For example, delta oscillation is associated with the deepest stages of dreamless sleep (also known as slow-wave sleep) and this has been reported also for learning,

motivation, and rewards in the brain (12). The role of theta oscillations is demonstrated in working memory processing, emotional arousal and fear conditioning (11, 17, 18). Alpha oscillations are involved in alertness, attention, working memory and short-term memory retention (19). Studies have linked beta oscillations with motor functions (20-24). More recently, beta oscillations are shown in maintaining accuracy of the task such as during decision-making (25, 26). Gamma oscillations have been demonstrated in a wide range of brain processes, including focused arousal, multisensory and sensorimotor integration, attention, memory formation, and conscious awareness (13, 27-29). The study of neuronal oscillations in the brain is important for understanding of not only healthy brain functions, but also brain dysfunctions epilepsy, schizophrenia, autism spectrum disorder, dementia, Alzheimer's disease and many more.

The conventional approach of analyzing scalp EEG data is to study event related potentials (ERPs) patterns over time. However, volume conductions and muscle artifacts that can mimic neural synchrony contaminate the ERPs. To resolve these, a recent shift in analysis is the transformation of EEG data into source space. Such source space not only provides better estimation of synchronized oscillatory activity but also substantially improves the spatial resolution of E/MEG measurements (15, 30). Several techniques have been proposed to achieve this goal. One of them is the low-resolution electromagnetic tomography (LORETA), which we will discuss with some details in the materials and methods section of chapter 3.

1.3 Network activity: directed connectivity measure

Over the past few years, multivariate neuronal recordings have become commonplace to investigate how different brain areas work together to achieve thoughts and behavior under different tasks and conditions, and how such coordinated brain activity disrupts in diseases.

Symmetric measure—mainly cross correlation, ordinary coherence spectra, and phase synchronization index—have been applied to evaluate how the different parts of the brain are functionally connected. These directionally symmetric measures are also often termed "functional connectivity measures", which are limited to evaluating functional interdependence of one neural system over another or vice versa (31). In recent years, asymmetric measures that deal with the information flow between the brain areas have been actively applied to functional neuroimaging data. These are often referred to " effective connectivity measures". One popular method is Granger causality, which is based on the theory of linear prediction. In 1956, Wiener (32) introduced an idea that if a time series is helpful in predicting another time series, the first time series is causal to the second. It was Clive Granger who implemented this idea using autoregressive models, and then applied this mathematical framework to investigate causal relations in econometric time series (33). The technique is henceforth termed as Granger causality (GC). Time domain GC (33, 34) was further generalized in frequency domain by Geweke (35, 36). Recent investigations have successfully applied the GC to infer the directed connectivity among the brain areas (37-39).

GC—a data-driven technique—can be mathematically expressed by considering simultaneously measured time series. Suppose we have two simultaneously recorded time series represented as, 1: $X_1(1)$, $X_1(2)$, ..., $X_1(t)$, ... and 2: $X_2(1)$, $X_2(2)$, ..., $X_2(t)$. GC spectral analyses can be used to examine the strengths, directions, and frequencies of interactions between such dynamic processes 1 and 2. The GC spectral method is a part of spectral interdependency methods. The measures of spectral interdependency are derived from the time series recordings of dynamic systems either by using autoregressive modeling (parametric method), or by using direct Fourier or wavelet transforms (nonparametric method) (40, 41). For a pair of multivariate

stationary processes (i. e., 1 and 2), there are three measures that characterize the spectral interdependency between these processes: total interdependence ($M_{1,2}$), GC (one-way effect or directional influence from the first process to the second process, $M_{1\to2}$, or from the second to the first, $M_{2\to1}$) and instantaneous causality (measure of reciprocity, $M_{1.2}$). In general, the total interdependence is the sum of directional influences and instantaneous causality frequency by frequency ($M_{1,2} = M_{1\to2} + M_{2\to1} + M_{1.2}$). The spectral interdependency measures are derived from the spectral matrix (S), and/or from the transfer function (H) and noise covariance matrix (Σ), which can be estimated by the parametric (prediction model building) (42) or nonparametric (model-free) approaches applied to these time series (40, 41). Σ is computed from the residual errors of the prediction models and the transfer function matrix H is constructed from the matrix inverse of the Fourier transforms of the coefficients in the prediction models. S, H and Σ can also be estimated by using the nonparametric spectral methods (40, 41) without explicitly fitting the time series $X_1(t)$ and $X_2(t)$ in autoregressive models. The GC spectrum from the second time series X_2 to the first time series X_1 (i.e., 2 to 1) at a frequency (f) is defined as

$$M_{2\to1}(f) = -\ln\left(1 - \frac{(\Sigma_{22} - \Sigma_{12}^2 / \Sigma_{11}) |H_{12}(f)|^2}{S_{11}(f)}\right) \tag{1.1}$$

In N EEG-source waveforms, the frequency-specific causal outflow (F) at a node i can be defined as,

$$F_i = \frac{1}{N-1}\sum_{j}^{N}(M_{i\to j} - M_{j\to i}) \tag{1.2}$$

Because of the unknown theoretical distributions of spectral GC, establishing statistical significance in these measures from experimental time series requires data resampling (surrogate) methods such as random permutation.

2 PERCEPTUAL DECISION-MAKING

Perceptual decision-making (PDM) deals with decision based on available sensory evidence. Even a very simple everyday decision—such as stopping a car at a red light or driving it at a green light—is believed to follow a systematic scheme that includes an encoding of sensory evidence, planning of actions, and mapping of sensory information into action plans. PDM has been extensively investigated using primate electrophysiological recordings (43-46), human neuroimaging (3, 47-51), and modeling experiments (52-56). In laboratory settings, the study of PDM has been mostly performed in both animals and humans using a stimulus categorization task with two or more forced-choice alternatives (1, 45). Those prior studies suggest that a distributed network of brain areas carry out PDM (57, 58). However, how a sensory signal enters and organizes within those brain areas before reaching the motor area for motor execution are still not well understood. The study of PDM is not only interesting in terms of choosing appropriate action from several alternatives but also possibly serving as a simple role model for more complex decisions in the long run. The present dissertation will focus on the following investigations as an attempt to understand PDM processes. More specifically, we will discuss oscillatory network dynamics of two distinct neurocognitive networks in PDM: the salience network and ventral temporal cortex-dorsolateral prefrontal cortex (VTC-DLPFC) network.

2.1 Salience network

The human brain makes sense of multiple internal and external inputs that compete for attention by determining which ones are salient (59, 60). The term salient here is understood in terms of a stimulus or an aspect of stimulus that is distinct from others (61-63). The brain dynamically selects specific sensory stimulus for additional processing from a wide stream of

incoming sensory inputs. Such saliency detection mechanisms in the brain are conceptualized in two ways. The first mechanism is a primitive, automatic, and bottom-up process that filters and amplifies the stimulus at multiple levels (64, 65). The second mechanism is a higher-order cognitive process that recruits content-specific information, stimulus selection and focusing, and enhances access to resources entailed for stimulus-driven goal-directed behaviors including making decisions (66-69). The salient mechanism that we discuss in this dissertation is the second mechanism of higher-order cognitive processes. Prior studies suggest that the salient features of the stimulus are primarily anchored in the right anterior insula (rAI), left anterior insula (lAI) and dorsal anterior cingulate cortex (dACC) (67, 69) in the brain, and a network of these brain areas is often referred as the salience network (SN). The SN contributes to a wide range of complex brain functions, including communication, social behavior, and sensory stimulus-guided goal-directed behaviors (61, 66, 70-72). Investigation of the SN has rapidly increased in last few years because emerging evidence shows that atypical engagement of the SN is a feature of several neuropsychiatric disorders, such as in autism spectrum disorder (73-77), schizophrenia (78-83), and frontotemporal dementia (84-87). Despite extensive study of the SN in both health and disease mentioned above, when and how a sensory signal enters and organizes within the SN before reaching the central executive network, including the prefrontal cortices, is still a mystery. Previous electrophysiological studies focused on individual nodes of SN, either on dACC or rAI, have reported of conflicting findings of the earliest cortical activity within the network. One group of studies argues that the dACC responds first to the salient event, and its interaction with the lateral prefrontal structures implement subsequent behavioral changes (88, 89). In contrast, the other literatures report that the rAI activates first to the salient event and then drives the SN (69, 90). I discuss our study that seeks to resolve these conflicting findings. The

details of the salience network dynamics in a perceptual decision-making task will be presented in chapter 3.

2.2 VTC-DLPFC network

Humans and nonhuman primates depend on their vision to detect, recognize, and classify the information present in their surroundings. This process includes a key mechanism in the brain called sensory processing. Prior studies suggest that sensory processing begins with the integration of available sensory evidence by lower order sensory areas in the brain (91-94). To better understand PDM mechanisms in visual processing, several studies have used direction of motion discrimination tasks (45, 91, 95) and others have used image categorization tasks (47, 96-98). One of them is categorizing the images of face and house. A face is a biologically distinct stimulus and its perception (and recognition) is considered a highly developed skill in cognitive development of humans, such as for acquiring the skills needed for social interaction and language (58, 99, 100). A house is also a stimulus category that has a direct connection with humans' life. Neuroimaging studies in humans suggest that a specific brain area within the ventral temporal cortex (VTC) responds more to faces than other visual objects (stimuli) and this brain area in the right hemisphere is often referred to as the fusiform face area (FFA) (47, 101, 102). In a similar vein, another brain area within the VTC activates more to houses than other visual stimuli, and this brain area in the left hemisphere is often called the parahippocampal place area (PPA) (98, 103-105). Studies mostly performed using fMRI (in seconds) reported that a higher order cortical area in the brain, named the dorsolateral prefrontal cortex (DLPFC), computes higher-level cognitive functions (106-108), including decision-making (1, 109). The DLPFC is proposed to compute a decision by comparing the relevant sensory evidence in the FFA and PPA for their respective choices (1). However, how a sensory signal enters and

organizes within this network has remained a mystery, specifically in the time-scales of human sensory perception and cognition. We discuss the detail of the VTC-DLPFC network dynamics during perceptual decision-making in chapter 3.

3 OSCILLATORY DYNAMICS OF THE: 1) SALIENCE NETWORK, AND 2) VTC-DLPFC NETWORK IN PERCEPTUAL DECISION-MAKING

3.1 Introduction

3.1.1 Salience network dynamics

Prior studies suggest that the salience network (SN)—the rAI, lAI and dACC in the brain (67, 69)—plays a crucial role in integrating sensory stimuli to initiate cognitive control (68), to implement and maintain task sets (110), and to coordinate behavioral responses (111). When and how a sensory signal enters and organizes within SN in a sensory-driven, goal-directed task is not understood. Such understanding can help predict impending perceptual decisions and task executions that involve the prefrontal cortex.

There are two main competing theories that explain the possible 'driving hub' of the SN. First theory proposes that the dACC monitors performance and signals the need for behavioral adaptation (88). Activity in the dACC signals the need for enhanced cognitive control, and interaction between the dACC and the lateral prefrontal structures implement subsequent behavioral changes (88, 89). In contrast, the second theory suggests that the rAI is a 'cortical outflow hub' of the SN and it coordinates a change in activity across multiple neurocognitive networks, such as the default mode network (DMN) and central executive network (CEN) (68, 90, 112). Diffusion tensor imaging (DTI) has demonstrated that the structural integrity of the white matter connection between the rAI and the dACC predicts behavioral and physiological

abnormalities after traumatic brain injury (112). Previous investigations using blood oxygenation level-dependent (BOLD) changes in fMRI showed that the rAI, not the dACC, drives the SN (69, 90) and further suggested that a change in the effective connectivity of the dACC was associated with behavioral adaptation (69). As BOLD hemodynamic responses are sluggish, it might in fact include processes that happen on longer time-scales (seconds) and, if so, the 'driving hub' of the SN might even change in millisecond time-scales of neuronal activities. The studies mentioned above (69, 89, 90, 113) reported conflicting findings of the earliest cortical activity—whether the dACC or the rAI drives the SN. Therefore, how a sensory signal enters SN and organizes within before reaching the prefrontal cortex for central executive processing remains a mystery, specifically in the time-scales of human sensory perceptions and cognitions. We seek to resolve these conflicting reports considering both anterior insulae and dACC in milliseconds time-scale. In particular, how the cortical areas of the SN interact, what the temporal flow of underlying overall activity in these cortical areas is, and what frequency band(s) of information flow binds the SN are largely unknown.

As the dACC, rAI and lAI are often co-activated, it has been hard to disentangle their causal features (69), specifically on longer time-scales such as from fMRI measures. In this study, we recorded human scalp electroencephalography (EEG), reconstructed source waveforms and investigated the causal relationships between the areas of the SN using spectral Granger causality (GC). In this EEG experiment, we used the standard face/house image categorization tasks and studied the temporal evolution of activity in the salience nodes and the patterns of oscillatory network activity flow binding SN nodes in a network. Adding noise to clear images, three noise levels of stimuli were created to examine whether a difficult task (or difficult decision) modulates the network activity flow.

3.1.2 VTC-DLPFC network dynamics

The human brain is organized in a large number of functionally specialized but widely disseminated cortical and sub-cortical areas. Sensory guided, goal-directed behaviors such as PDM—the process that includes encoding of sensory evidence, planning of actions and mapping of sensory information into action plans (1)—entails the flexible interactions between task-relevant areas, but the underlying neural mechanisms regulating such interactions are poorly understood. Here we seek to investigate the large-scale neural oscillatory networks involved in visual perceptual decisions.

Sensory processing, including visual processing, comprises encoding of sensory evidence by lower order sensory areas (91-94). Neuroimaging studies in the human have repeatedly demonstrated that the areas of ventral temporal cortex (VTC) are involved for encoding and processing visual information, specifically the right fusiform face area (FFA) and the left para-hippocampal place area (PPA) for faces and houses, respectively (47, 105). The FFA and PPA also process other forms of visual objects, such as birds, fish and insects (98, 114, 115) emphasizing the role of bilateral interaction in visual processing (116, 117). In PDM literature, the dorsolateral prefrontal cortex (DLPFC) has been proposed to read available sensory evidence from the lower order sensory areas (1, 47, 95, 118-121), although the underlying neural mechanisms related to such interactions are not well understood. Previous neuroimaging studies have mostly focused on sluggish BOLD-fMRI (1, 47, 119) to investigate the network features between the FFA, PPA and DLPFC. Therefore, how these brain areas interact in a millisecond time-scale, what the temporal flow of underlying overall activity in these brain areas is, and what frequency bands of information flow bind them in the network are largely unknown to date.

Electrophysiological studies followed by source localization have reported that the FFA responds to a face at ~150-180 ms after stimulus onset (122, 123). These studies provide some clue about the temporal activation pattern in the VTC—the FFA and the PPA. A recent EEG investigation (120) provided a clue that the DLPFC activated at ~170-210 ms after stimulus onset, although it was in the somatosensory domain. A systematic source-level activation pattern of temporal evolution in the FFA, PPA and DLPFC for visual stimuli, especially face/house stimuli, still needs to be resolved. Based on the available literature discussed above, we hypothesized that visual processing of the face/house stimuli involves a network that links the lower order sensory areas (the FFA and the PPA) and the higher order brain area in the prefrontal cortex, the DLPFC. We designed an EEG experiment by using the standard face/house discrimination task to test this hypothesis. Furthermore, we added noise on these stimuli to test whether a difficult task (difficult decision) is associated with additional network activity among the FFA, PPA and DLPFC.

3.2 Materials and Methods

3.2.1 Participants

Twenty-six neurologically healthy human volunteers (21 males, 5 females) of age ranged from twenty-two to thirty-eight years (mean: 26.3 years, standard deviation: 4.7 years) participated in this study. A written informed consent was collected from the participants prior to data collection. The Institutional Review Board of Georgia State University approved the experimental protocol. Three participants were excluded from the final analyses because of behavior performance and/or unmanageable artifacts and noise present in their EEG data.

3.2.2 Stimuli

We used a total of twenty-eight images of faces and houses (14 images of each category). Face images were from the Ekman series (124). Fast Fourier transforms (FFT) of these images were computed, providing twenty-eight magnitude and twenty-eight phase matrices. The average magnitude matrix of this set was stored. Stimulus-images were produced from the inverse FFT (IFFT) of average magnitude matrix and individual phase matrices. The phase matrix used for the IFFT was a linear combination of the original phase matrix computed during the forward Fourier transforms and a random Gaussian noise matrix. The resulting images all had an identical frequency power spectrum (corresponding to the average magnitude matrix) with graded amounts of noise as done in previous studies (1, 47, 125). Finally, the stimuli consisted of three different noise-levels: 0%, 40% and 55% (i.e., clear stimuli, 40% noisy stimuli, and 55% noisy stimuli). The E-Prime 2.0 software was used to display the stimuli and control the task sequences.

3.2.3 Experimental design

Prior to the experimental task, the participants were briefly explained about the task paradigm. Participant sat in a dark room (the only source of light was from the experimenter's computer screen) and viewing distance was ~60 cm (chin rest). Figure 3.1 shows a schematic of experimental paradigm used. The experiment consisted of 4 blocks of 168 trials (672 trials in total with 224 trials for each noise level). On each trial, a small fixation cross ('+' in the middle of the screen) was presented for 500 ms. Then a stimulus was presented for 150 ms, followed by a black screen with a question mark ('?') for 1500 ms, during which time participants were allowed to indicate their decision (either face or house) by a keyboard button press. Responses after that delay were considered incorrect.

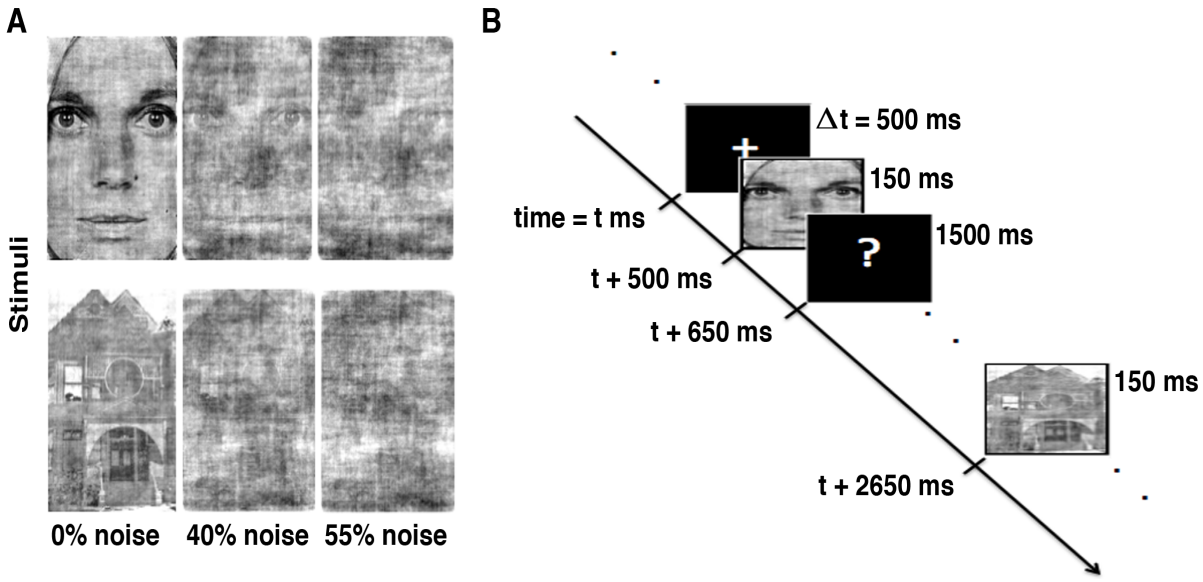

Figure 3.1 Experimental design.
A) Stimuli with three noise-levels, B) task paradigm: stimuli were presented for 150 ms, followed by black screen with question mark ('?') for 1500 ms during which time participants responded with a keyboard button press.

3.2.4 Data acquisition and preprocessing

EEG data were acquired with a 64-channel EEG system from Brain Vision LLC (http://www.brainvision.com). The analog signal was digitized at 500 Hz. The impedances of each electrode were kept below 10 kΩ, and the participants were asked to minimize blinking, head movements, and swallowing. EEG data were band-pass filtered between 1 and 100 Hz, and notch filtered to remove 60 Hz AC-line noises. The eyes blinking were removed using independent component analysis (ICA)-based ocular correction. Data from bad electrodes were discarded and replaced, when appropriate, by spatial interpolation from the neighboring working electrodes. These preprocessing steps were done using Brain Vision Analyzer 2.0 (http://www.brainproducts.com).

3.2.5 Data Analysis

The preprocessed EEG data were analyzed in the following main steps:

3.2.5.1 Computation of ERPs

Continuous EEG data were segmented into trials of 400 ms duration (post-stimulus: 0 to 400 ms) based on the stimulus onset times as a reference. The trials that had three standard deviations below or above the global mean across time in each subject were considered as outliers (126) and they were discarded from the subsequent analysis.

3.2.5.2 EEG-source and single-trials source waveforms reconstruction

All correct trials (ERPs of correct percept) from all three noise conditions were grand averaged and imported to BESA software version 5.3.7 (www.besa.de) to reconstruct EEG sources. We used the low resolution electromagnetic tomography (LORETA) (127), which is also referred as Laplacian weighted minimum norm, to reconstruct the EEG sources. LORETA is an extensively used source localization technique in EEG studies for both cortical and deep brain structures (10, 122, 128-130), including insula and hippocampus (10, 129, 130). Depth weighting strategy implemented in LORETA overcomes the problem of surface-restricted localization methods, such as minimum norm estimates (MNE) (131-133). LORETA uses the Talairach atlas coordinates of Montreal Neurological Institute (MNI) MRI average of 305 brains and computes the inverse solution at 2394 voxels with spatial resolutions of 7 mm (131, 134). It is based on the assumption that the smoothest of all possible neural activity distributions is the most plausible one. This assumption is also supported by electrophysiology, where neighboring neuronal populations show highly correlated activity while EEG-LORETA results are the activity rendered by neighboring voxels with maximally similar activity (122, 132, 135). Locations of sources can be constrained to the cortical surface and their orientations

perpendicular to the local cortical surface based on neurophysiological information that the sources of EEG are postsynaptic currents in cortical pyramidal cell, and that the direction of these currents is perpendicular to the cortical surface (136, 137). Peak activities of these sources were marked as the network nodes for connectivity analyses. Using single-trials EEG data, we fitted dipoles at the locations of peak activation of localized sources of SN—the rAI, lAI, and dACC based on our hypothesis—with dipole orientation presented in Table 1. Similarly, we also fitted dipoles at the location of peak activation of localized sources of VTC-DLPFC network: that is, at the FFA, PPA, and DLPFC (Table 2). The single-trials source signals were then extracted using a four-shell spherical head model and a regularization constant of 1% for the inverse operator. These source signals were used for the connectivity analyses.

3.2.5.3 Power and Granger causality spectral analyses

The power spectra can be computed using parametric and nonparametric approaches (4, 40, 41). To find the proper model order (which was four), we compared the spectral power from both parametric and nonparametric approaches at different model orders and picked the model order that rendered the lowest power difference between two approaches.

As the SN nodes showed a dominant activation at ~75-140 ms (as shown in Table 1), we tried to cover dominant activation time frame in a single time frame while computing the power and GC spectra at different time windows. We calculated the power and GC spectra from source waveforms of SN nodes in four consecutive time frames: 0-75 ms, 75-150 ms, 150-225 ms, and 225-300 ms to uncover how the nodes and network activity changes with time. Besides time frame wise GC calculations, we also computed GC spectra using a sliding window technique (138, 139) by selecting a window size of 50 ms and sliding it every 2 ms to further observe how GC patterns change over time. The threshold value of GC, for statistical significance, was

computed from surrogate data (that is, from SN nodes) by using permutation tests and a gamma-function fit (120, 140) under a null hypothesis of no interdependence at the significance level $p < 10^{-4}$. The causal outflow at a node (See Eq. 1.2) is computed as the total GC flowing out from a node minus total GC flowing in to that node in beta band (13-30 Hz).

For VTC-DLPFC network, as the FFA, PPA, and DLPFC showed dominant activation at ~130-240 ms (as shown in Table 2), we tried to cover dominant activation time frame of those nodes in a single time frame while computing the power and GC spectra at different time windows. We calculated the power and GC spectra from source waveforms of FFA, PPA, and DLPFC in three consecutive time frames: 0-125 ms, 125-250 ms, and 250-375 ms to uncover how the nodes and network activity changes with time. Besides time frame wise GC calculations, we also computed GC spectra using a sliding window (138, 139) to further examine how GC patterns change over time. The threshold value of GC, for statistical significance, was computed from surrogate data (that is, from FFA, PPA, and DLPFC) by using permutation tests and a gamma-function fit (120, 140) under a null hypothesis of no interdependence at the significance level $p < 10^{-3}$. The causal outflow at a node (See Eq. 1.2) is computed as the total GC flowing out from a node minus total GC flowing in to that node in beta band (13-30 Hz) and gamma (30-100 Hz), respectively.

3.2.6 Brain-behavioral correlation.

The response time (RT) of each participant for each stimulus was recorded. To see the brain-behavioral correlation with the increase in noise level in stimuli, RTs were converted into z-scores and plotted with GC. The relationship between GC and RT was tested using both Spearman's rank correlation and Pearson's correlation. If $p < 0.05$ for both, the correlation was considered significant. The results reported here are in terms of Spearman's rank correlation.

3.3 Results

3.3.1 Behavioral results

The mean performance percent—a ratio of the number of correct responses to the total number of responses multiplied by 100 and averaged over all participants—was highest for stimuli with 0% noise level (mean: 96.80%, standard deviation: 0.71%) compared to the stimuli with 40% noise level (mean: 92.68%, standard deviation: 1.54%) and 55% noise level (mean: 69.67%, standard deviation: 2.74%). Repeated measures analysis of variance (RMANOVA) (141) showed the significant effect of noise levels (task difficulty) on the performance ($F_{(2,44)}$ = 150.43, p = 0.000003) and the response time (RT) ($F_{(2,44)}$ = 132.74, p = 0.000000). Pair t-test post hoc analyses followed by false discovery rate (FDR) multiple comparisons (142) further revealed that performance significantly decreased with the increase in noise level ($p < 10^{-3}$; FDR-corrected). The mean RT—the time taken to indicate the decision by pressing a keyboard button press and averaged over all participants—was shorter for stimuli with 0% noise level (mean: 434.02 ms, standard deviation: 22.09 ms) compared to the stimuli with 40% noise level (mean: 484.28 ms, standard deviation: 22.66 ms) and 55% noise level (mean: 565.70 ms, standard deviation: 25.73 ms). Pair t-test post hoc analyses followed by FDR multiple comparisons further illustrated that the RT significantly increased with the increase in noise level ($p < 10^{-6}$; FDR-corrected) as shown in Figure 3.2.

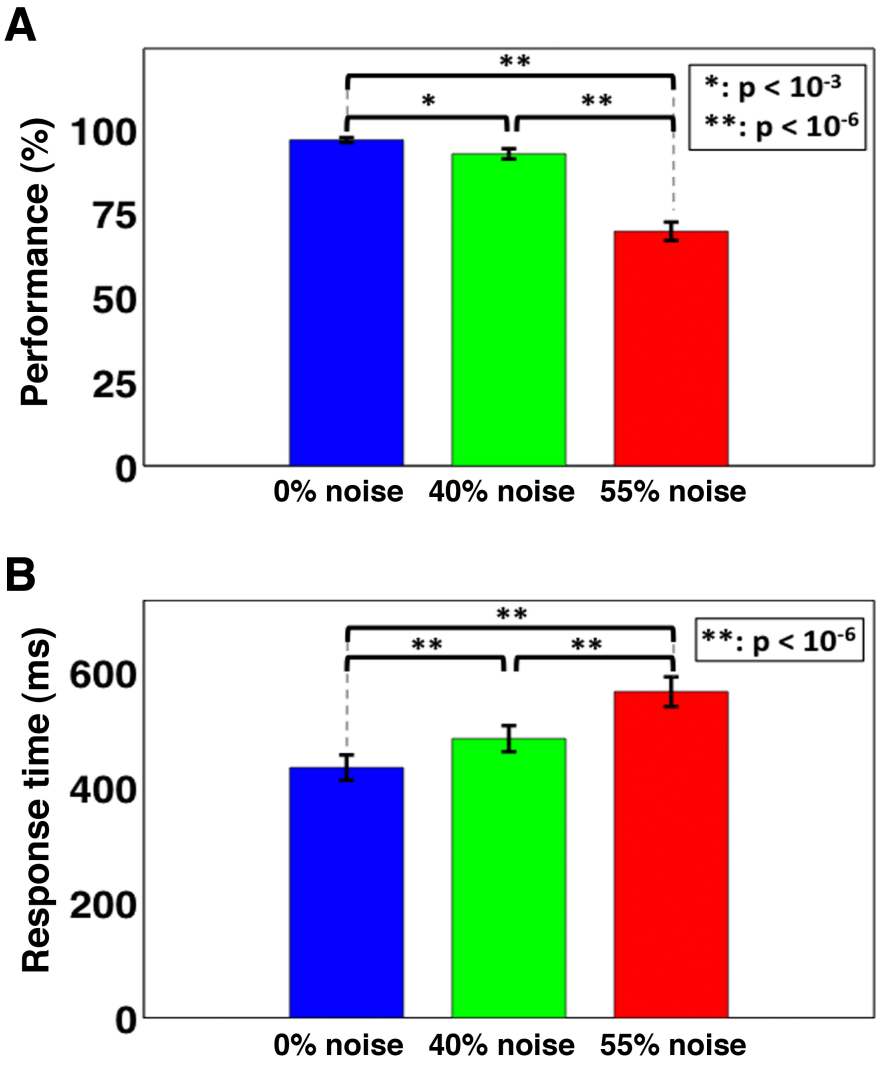

Figure 3.2 Behavioral responses for all three noise-levels.
A) Behavioral accuracy (performance %) significantly decreased, but B) the response time significantly increased with an elevated noise in the stimuli.

3.3.2 Brain results

3.3.2.1 Salience network dynamics

The average ERPs for correct decisions were used to compute localized sources (inverse solutions) in LORETA (127). Figure 3.3 shows the locations of the peak source activity (marked by cross-hairs) in time (first row), and the locations and orientations of

fitted dipoles in the SN nodes (second row) to obtain the single-trials source waveforms.

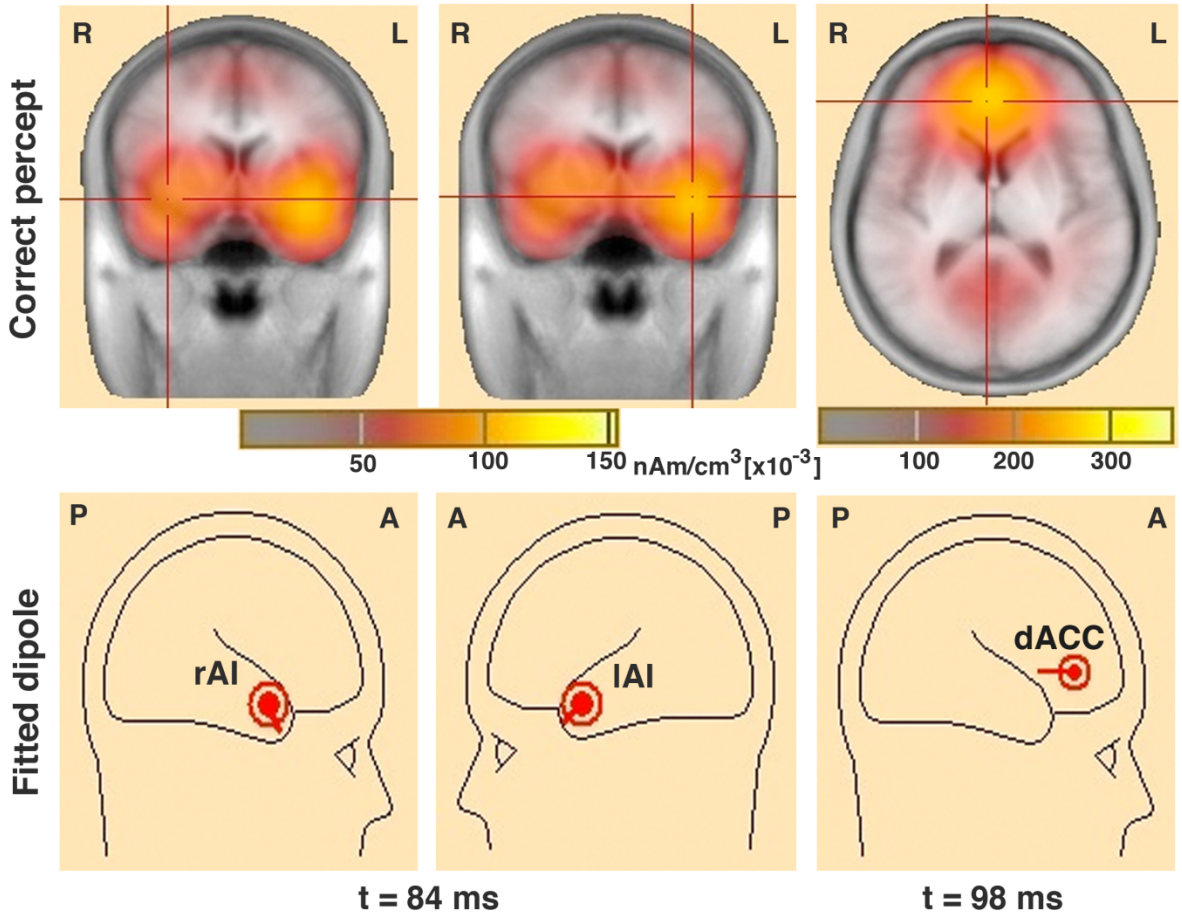

Figure 3.3 Spatiotemporal profiles of peak source-level brain activity over the SN nodes.
The first row shows peak source-level brain activity over the rAI and the lAI at 84 ms, and the dACC at 98 ms, and the second row shows the fitted dipoles on those nodes.

The earliest peak activation occurred in the visual area (BA17/18: V_1/V_2) at ~60 ms. The activation in the SN nodes started at ~76 ms after the stimulus onset. Maximum peak activations occurred at ~84 ms in the rAI and lAI (BA47/13), which was followed by activation in the dACC (BA32) at ~98 ms. Table 1 list the ERP source

locations, dipole orientations of SN nodes in the source model, and dominant activation time frames of cortical sources. The dipoles fitted at the locations and orientations shown explained approximately 80% of the variance in the EEG signal for trials with correct responses.

We computed power spectra using the wavelet technique (Figure 3.4) and GC spectra using a sliding window (Figure 3.5) to see the activity over the entire time. To further access how power and GC spectra change over time, we then performed calculations at four time frames. Power spectra computed in four consecutive time frames—TF1: 0 ms to 75 ms, TF2: 75 ms to 150 ms, TF3: 150 ms to 225 ms, and TF4: 225 ms to 300 ms—at the rAI, lAI, and dACC showed peak activity in beta band when the participants viewed clear stimuli (see Figure A.1).

Table 1 Anatomical location, dipole orientation, and dominant activation timeframe of the SN nodes.

Brain areas	Talairach coordinates x, y, z (mm)	Dipole orientations x, y, z	Dominant activation period (ms)
Right anterior insula (rAI)	35.0, 9.0, -7.0	0.9, 0.3, -0.4	78 – 142
Left anterior insula (lAI)	-33.0, 11.0, -8.0	-0.9, 0.4, -0.3	76 – 144
Dorsal anterior cingulate cortex (DACC)	4.0, 38.0, 13.0	0.1, 1.0, 0.0	76 – 146

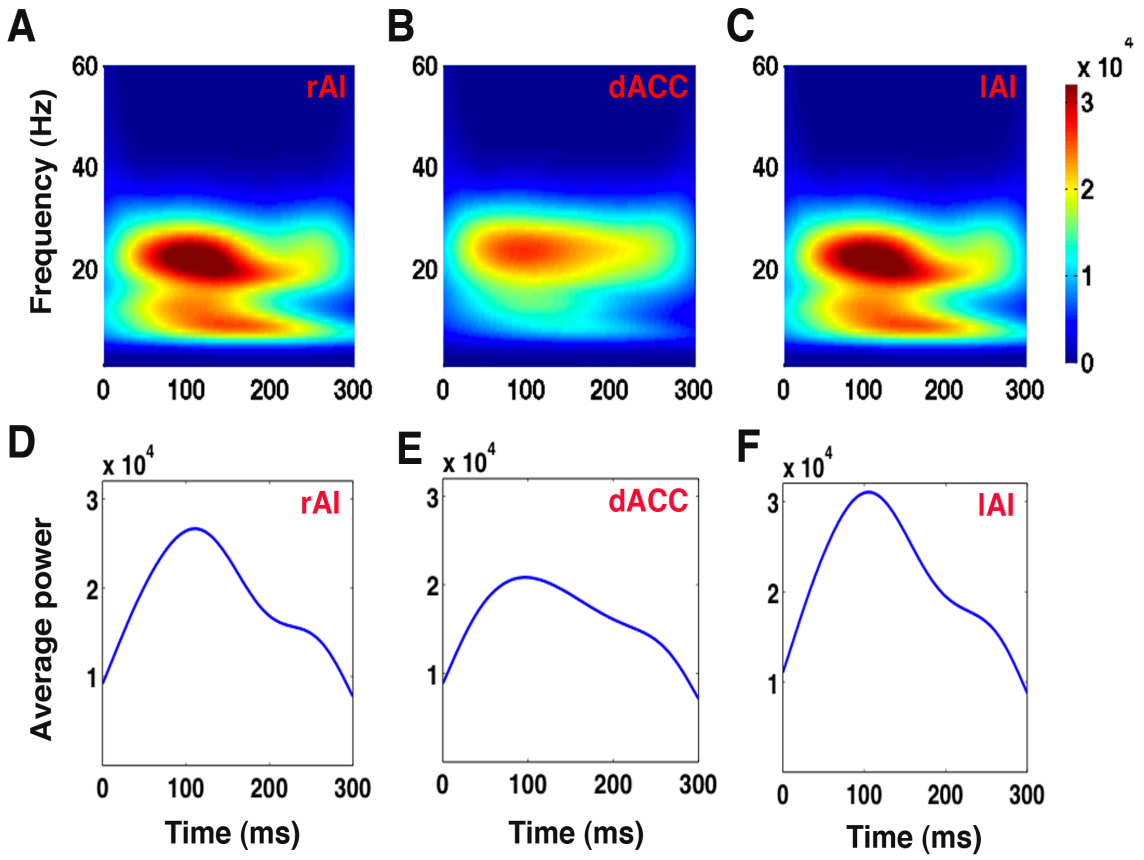

Figure 3.4 Power spectra of the SN nodes as a function of time and frequency for stimuli with 0% noise.
The first row (panels A, B, C) shows wavelet power at the rAI, dACC, and lAI for clear stimuli (0% noise) with peak beta activity in around 75 ms to 150 ms compared to other time frames, and the second row (panels D, E, F) represents the average power (averaged over beta band) showing peak activity at ~100 ms in the rAI, dACC, and lAI.

Figure 3.6 shows power comparison of nodes of the SN among TF1, TF2, TF3 and TF4. Overall power over the SN nodes in TF2 is significantly higher compared to other TFs. GC spectra were computed to assess the oscillatory network interactions among the SN nodes.

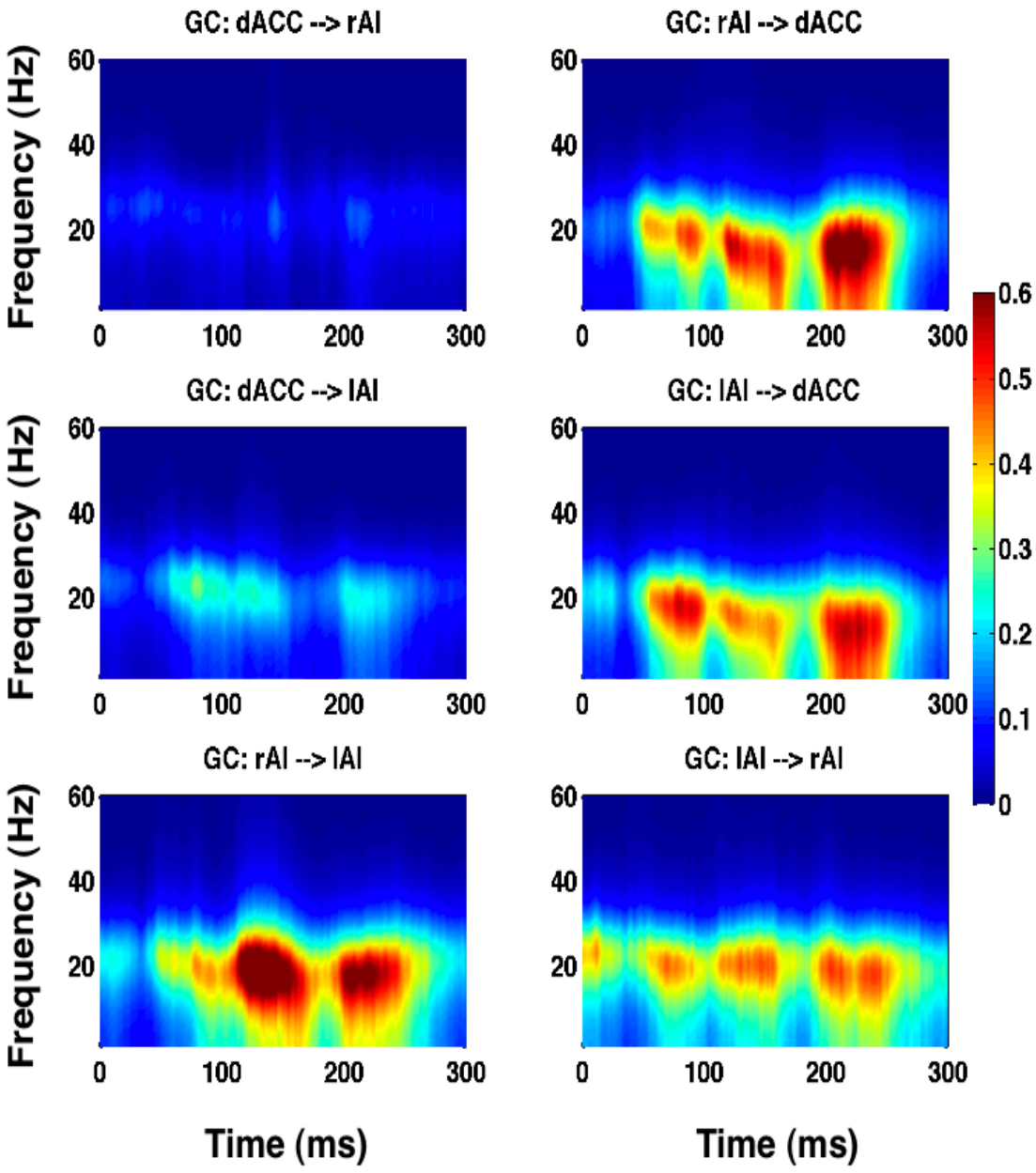

Figure 3.5 Granger causality spectra among the SN nodes as a function of time and frequency for stimuli with 0% noise.

Granger causality (GC) spectra as a function of entire time window (sliding time in milliseconds) and frequency for stimuli with 0% noise-level illustrating beta band activity. The first row shows GC between dACC-rAI pair, second row shows GC between dACC-lAI pair, and third row displays GC between rAI-lAI pair.

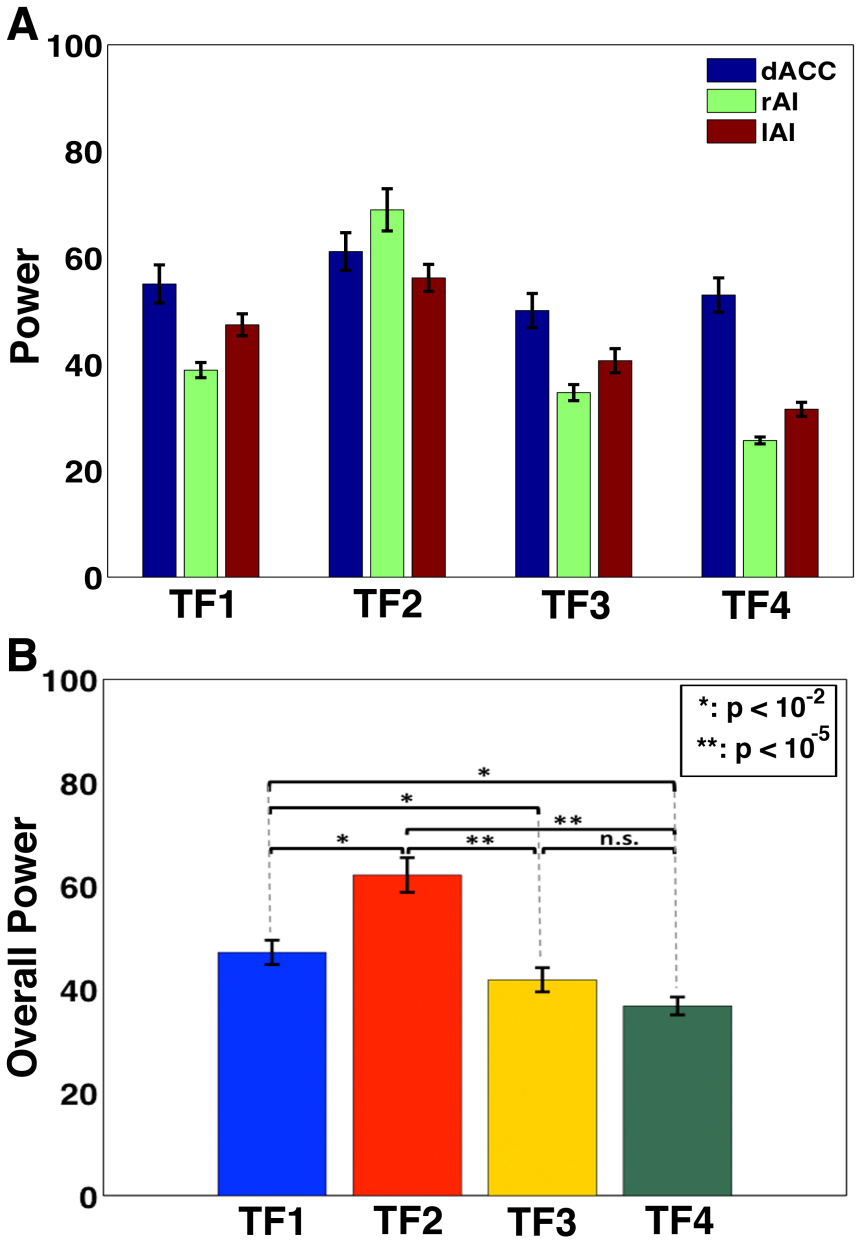

Figure 3.6 Power comparison of the SN nodes among four consecutive time frames for stimuli with 0% noise.

A) Power comparison the SN nodes among four consecutive time frames (TF1: 0 ms to 75 ms, TF2: 75 ms to 150 ms, TF3: 150 ms to 225 ms, and TF4: 225 ms to 300 ms) for 0% noise-level. B) Average power over the SN nodes in TF2 is significantly higher compared to other TFs (p represents significant statistical value; n.s. represents not significant).

Figure 3.7 presents GC spectra as a function of frequency, where horizontal lines represent statistically significant threshold value. Beta band network interactions between the SN nodes are enhanced in the TF2 (second column) compared to the rest of the TFs (other columns).

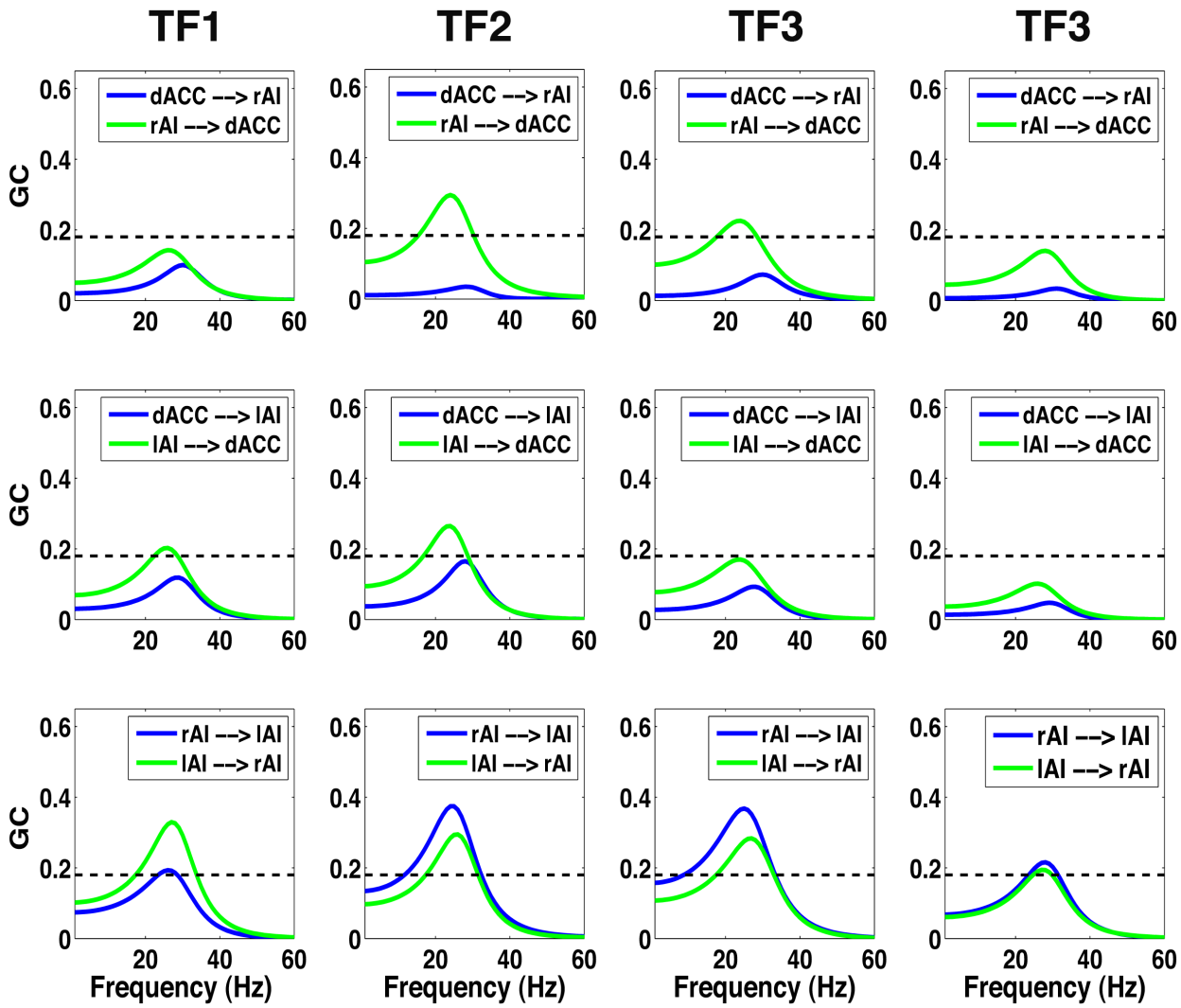

Figure 3.7 Granger causality spectra between all possible pairs of the SN nodes at four consecutive time frames for stimuli with 0% noise.
Granger causality (GC) spectra of all possible pairs between the rAI, lAI, and dACC for stimuli with 0% noise-level at four consecutive time frames (TF1: 0 ms to 75 ms, TF2: 75 ms to 150 ms, TF3: 150 ms to 225 ms, and TF4: 225 ms to 300 ms) mentioned at top of each column.

The overall connectivity strength of TF2 and TF3 were significantly higher than those of others, with the biggest strength in TF2 (Figure 3.8A). Causal outflow calculations in TF2 (the time frame of biggest overall connectivity strength) further showed the rAI as a main 'cortical outflow hub' and the dACC as a main 'cortical inflow hub' within the SN (Figure 3.8B).

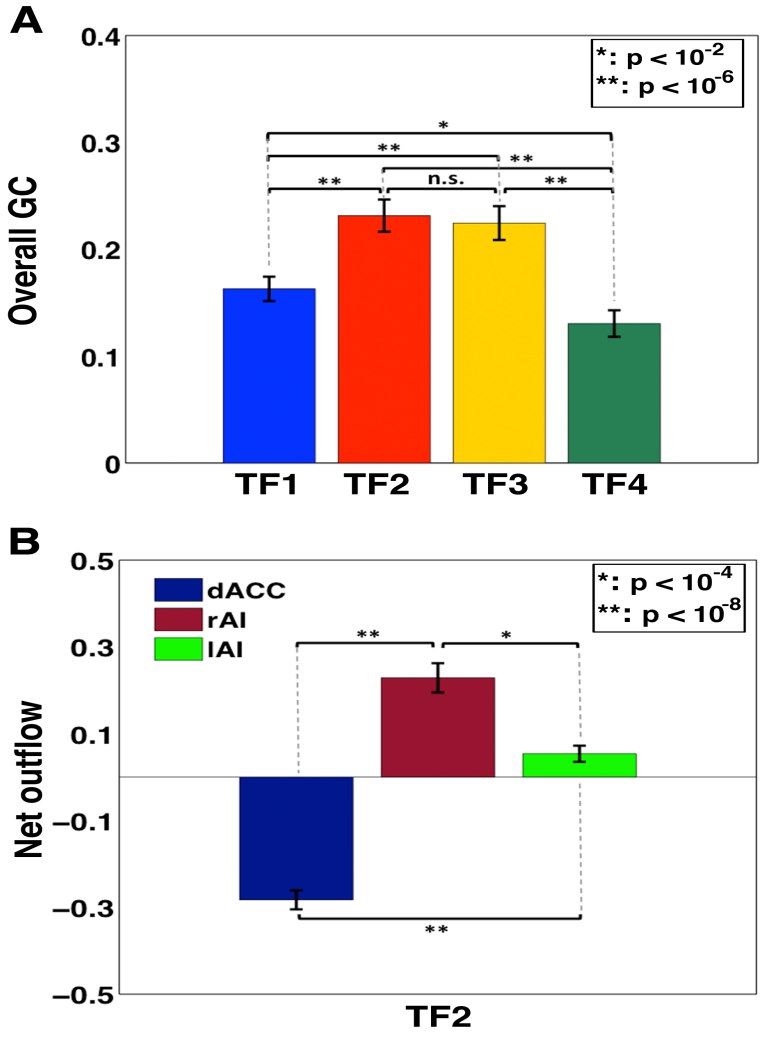

Figure 3.8 Comparison of overall Granger causality and calculation of net outflow for stimuli with 0% noise.
A) Overall GC connectivity strength among SN nodes is higher in TF2 than others (TF1: 0 ms to 75 ms, TF2: 75 ms to 150 ms, TF3: 150 ms to 225 ms, and TF4: 225 ms to 300 ms) for 0% noise-level, and B) net GC outflow of the SN nodes computed at the

time frame of highest connectivity strength (TF2) showed the rAI as a main outflow hub (p indicates statistically significant difference).

Power spectra were also computed for TF1, TF2, TF3, and TF4 at the rAI, lAI, and dACC when participants viewed the stimuli with 40% and 55% noise-levels (see Figures A.2, A.4). Power spectra calculations also showed peak activity in the beta band. GC spectra were calculated to see the oscillatory network interactions among the SN nodes in the entire time window (Figure 3.9 and Figure 3.10). GC spectra were computed at four time frames to better assess the time dependence of the oscillatory network interactions among the SN nodes.

Beta band network interactions among the SN nodes were suppressed for noisy stimuli compared to clear stimuli in the TF2 (see second columns of Figures 3.7, A.3, A.5). Overall causal interactions among the SN nodes were further compared between noise-levels by paired t-tests to assess the significant effect of task difficulty. We found that the overall information flow was significantly suppressed when the noise-level was elevated from 0% to 40%. Overall causal interactions were further significantly suppressed in the SN when the noise-level was elevated from 40% to 55% (Figure 3.11).

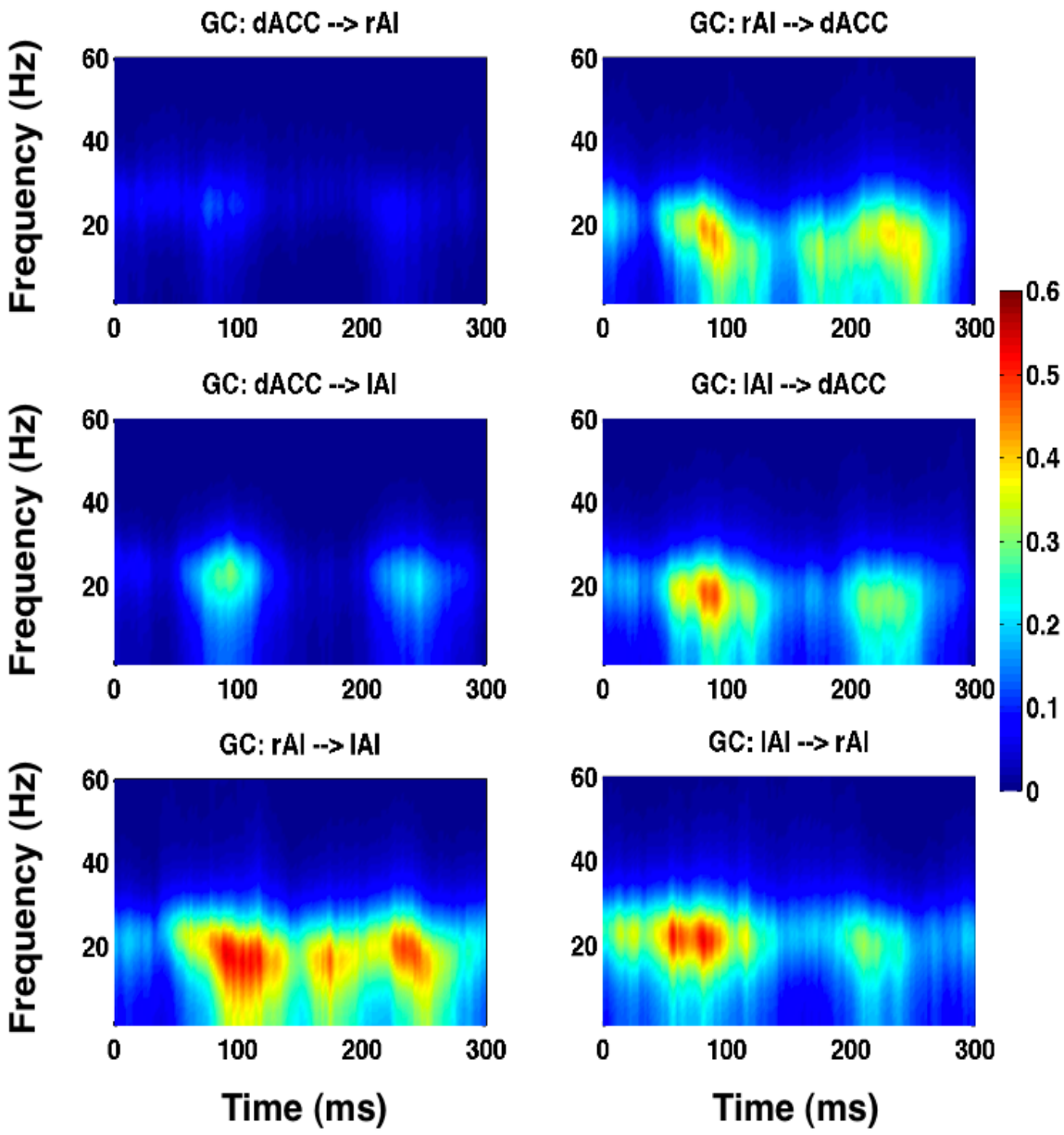

Figure 3.9 Granger causality spectra among the SN nodes as a function of time and frequency for stimuli with 40% noise.
Granger causality (GC) spectra as a function of entire time window (sliding time in milliseconds) and frequency for stimuli with 40% noise-level illustrating beta band activity. The first row shows GC between dACC-rAI pair, second row shows GC between dACC-lAI pair, and third row displays GC between rAI-lAI pair.

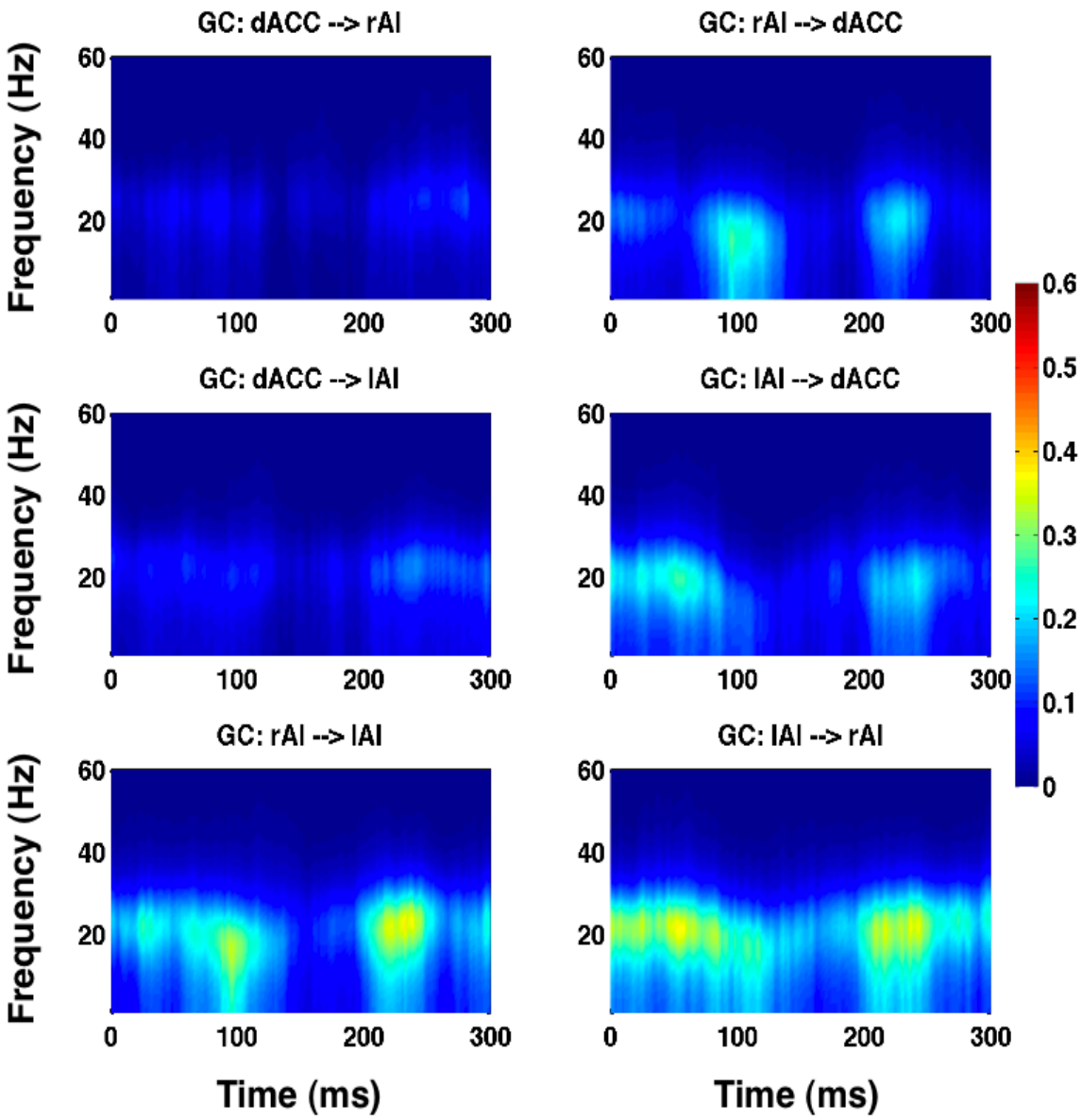

Figure 3.10 Granger causality spectra among the SN nodes as a function of time and frequency for stimuli with 55% noise.
Granger causality (GC) spectra as a function of entire time window (sliding time in milliseconds) and frequency for stimuli with 0% noise-level illustrating beta band activity. The first row shows GC between dACC-rAI pair, second row shows GC between dACC-lAI pair, and third row displays GC between rAI-lAI pair.

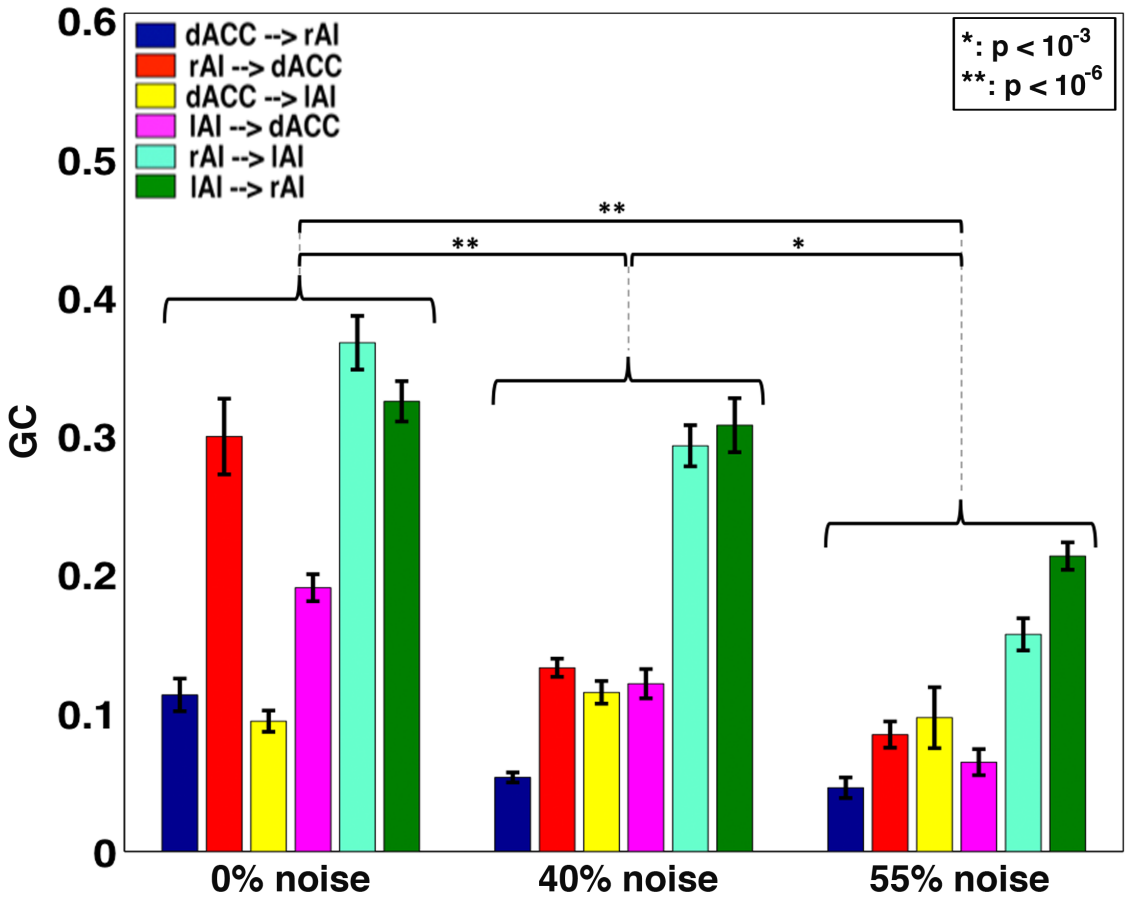

Figure 3.11 Comparison of Granger causality strengths among noise levels.
Granger causality (GC) connectivity strengths among SN nodes among all three noise-levels in the TF2: 75-150 ms. Overall connectivity strength is significantly suppressed with an elevated noise in the stimuli (p indicates statistically significant difference).

The difficulty levels—expressed in terms of behavior response times—were found to be significant and negatively correlated with the measures of network activity for all possible connections between cortical areas of the SN, except for the dACC to lAI flow, in the TF2 (75-150 ms). The correlation coefficient (r) and the corresponding p-value of all possible connections are presented in Figure 3.12 (see Figures A.6, A.7 and A.8 for other TFs).

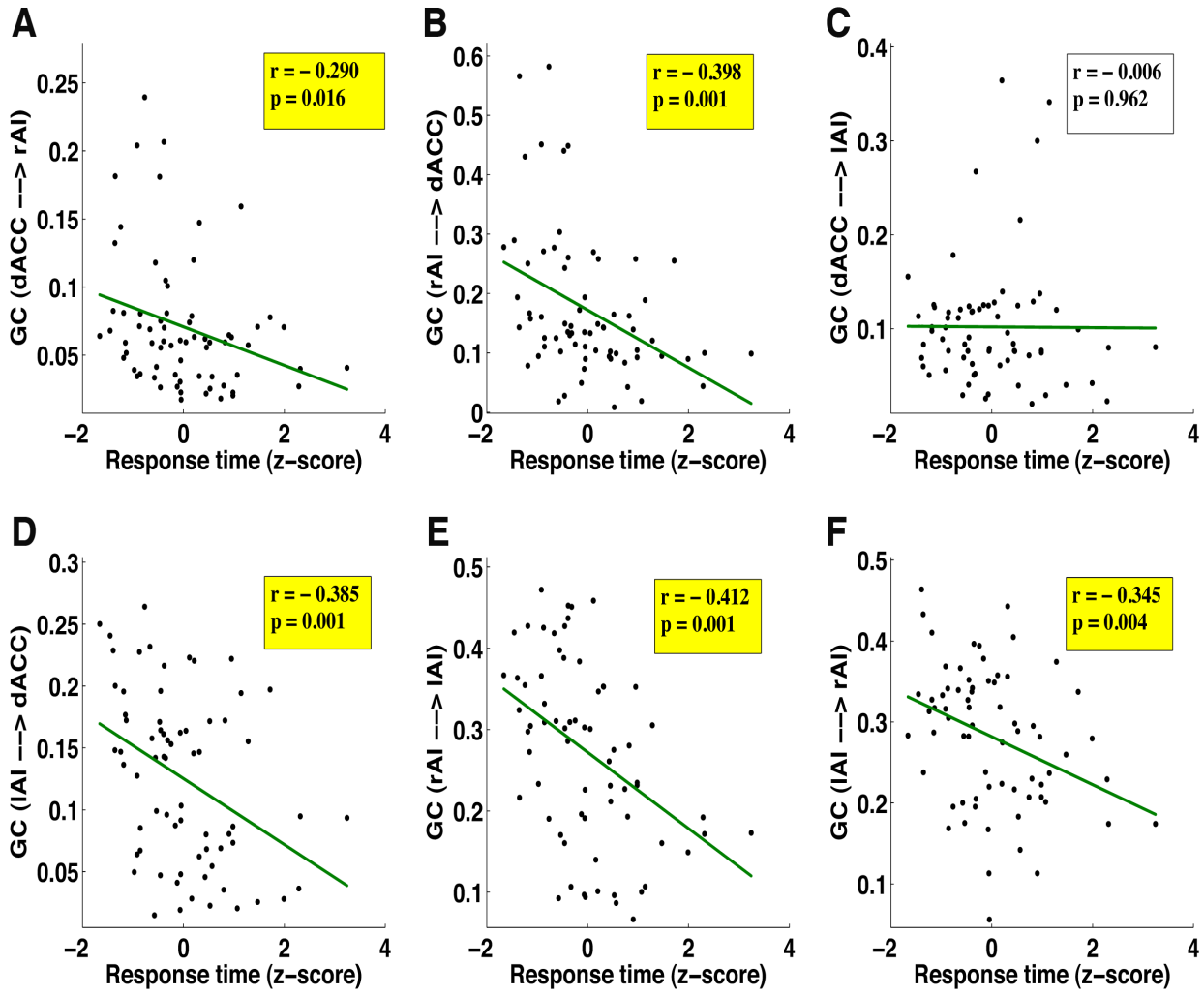

Figure 3.12 Relation between Granger causality and response time.
Granger causality (GC) decreased with difficulty level of tasks, expressed in terms of response time of all three noise-levels, in TF2: 75-150 ms (r represents correlation coefficient and $p < 0.05$ represents statistically significant correlation).

3.3.2.2 VTC-DLPFC network dynamics

The average ERPs for correct responses were computed for clear stimuli (faces and houses, separately) to examine the related ERP features over occipital-temporal channels. Figure 3.13A is Brain Products 10-20 EEG system showing standard channel information. We found first negative peak at ~170 ms so called N170-component. The N170-component of ERPs over the right occipital-temporal channels (P_6, P_8 and PO_8) and left occipital-temporal channels (P_5, P_7

and PO_7) showed relatively right and left lateralized activity for clear faces and clear houses, respectively. Moreover, ERPs for clear faces are relatively higher than that of houses.

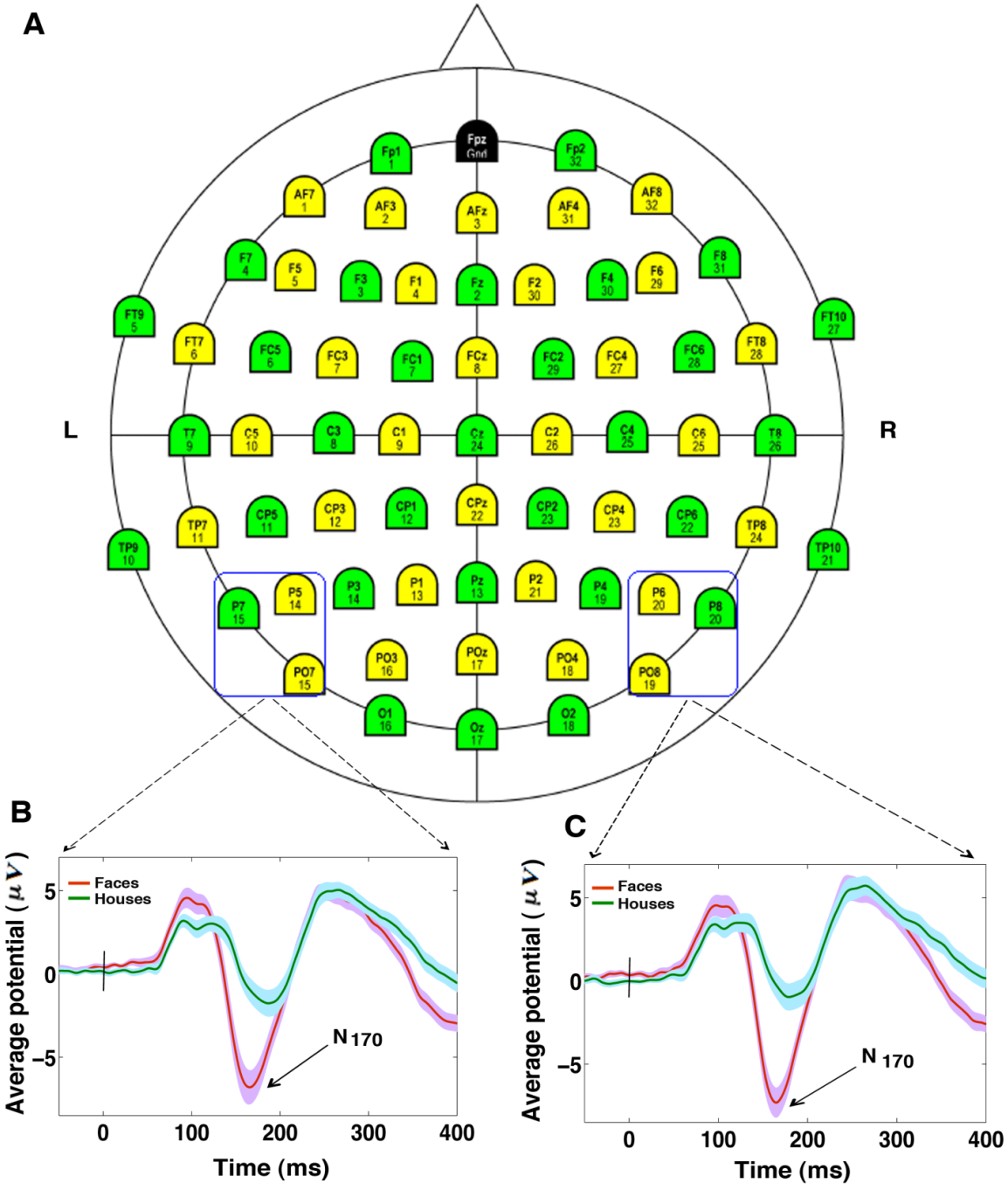

Figure 3.13 Event related potentials over the occipital-temporal channels.
A) Brain Products 64-channel EEG montage, B) the N170-component of ERPs over the left occipital-temporal channels, and C) the N170-component of ERP over the right occipital-temporal channels.

The average ERPs for correct responses were used for the inverse technique, LORETA (127), to find the cortically localized sources. Figure 3.14 shows the location of peak source activity (shown by crossing of lines) as it traversed the cortical surface (first row), and the locations and orientations of fitted dipoles used to obtain the single-trials source waveforms (second row). The earliest peak of cortical activity occurred in the visual area (BA17/18) at ~60 ms after stimulus onset. We observed activation in the areas of ventral temporal cortex (BA37: the right FFA and the left PPA) at ~160 ms, and finally in the left DLPFC (BA9) at ~224 ms. Table 2 lists the ERP source locations, dipole orientations of the source model, and dominant activation time frame of cortical sources. The dipoles fitted at the locations and orientations shown explained approximately 80% of the variance in the EEG signal for trials with correct responses.

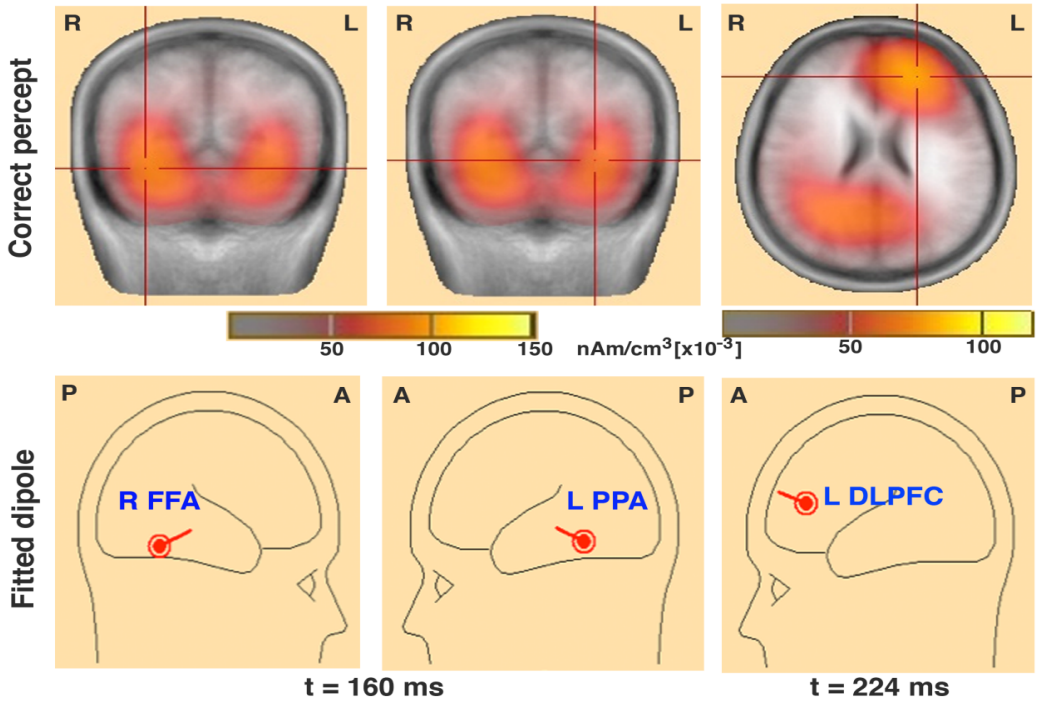

Figure 3.14 Spatiotemporal profiles of activity over the VTC-DLPFC nodes.
The first row shows peak activity in the FFA and PPA at 160 ms, and in the DLPFC at 224 ms, and the second row shows the fitted dipoles at those nodes.

We computed GC spectra using a sliding window (Figure 3.15) to see the activity over the entire time. To further access how power and GC spectra changes over time, we then performed calculations at three timeframes. Power spectra computed in the three consecutive time frames—TF1 (0-125 ms), TF2 (125-250 ms), and TF3 (250-375 ms)—at the DLPFC, FFA and PPA showed peak activity in the beta band and gamma band when the participants perceived clear stimuli (0% noisy stimuli). Figure 3.16 shows the power computed at these nodes in the TF1, TF2 and TF3. Overall power over these nodes was compared among these TFs using paired t-test. We found that beta power was significantly higher in TF2 compared to other TFs, however gamma power was significantly higher in TF1. GC spectra were calculated to assess the oscillatory neural network interactions among these nodes.

Table 2 Anatomical location, dipole orientation, and dominant activation timeframe of the VTC-DLPFC nodes.

Brain areas	Talairach coordinates x, y, z (mm)	Dipole orientations x, y, z	Dominant activation period (ms)
Right fusiform face area (R FFA)	36.0, -47.0, -16.0	0.6, -0.7, -0.4	140 – 190
Left parahippocampal place area (L PPA)	-30.0, -45.0, -10.0	-0.5, -0.8, -0.3	145 – 200
Left dorsolateral prefrontal cortex (DLPFC)	-21.0, 39.0, 28.0	-0.3, 0.9, 0.4	210 – 245

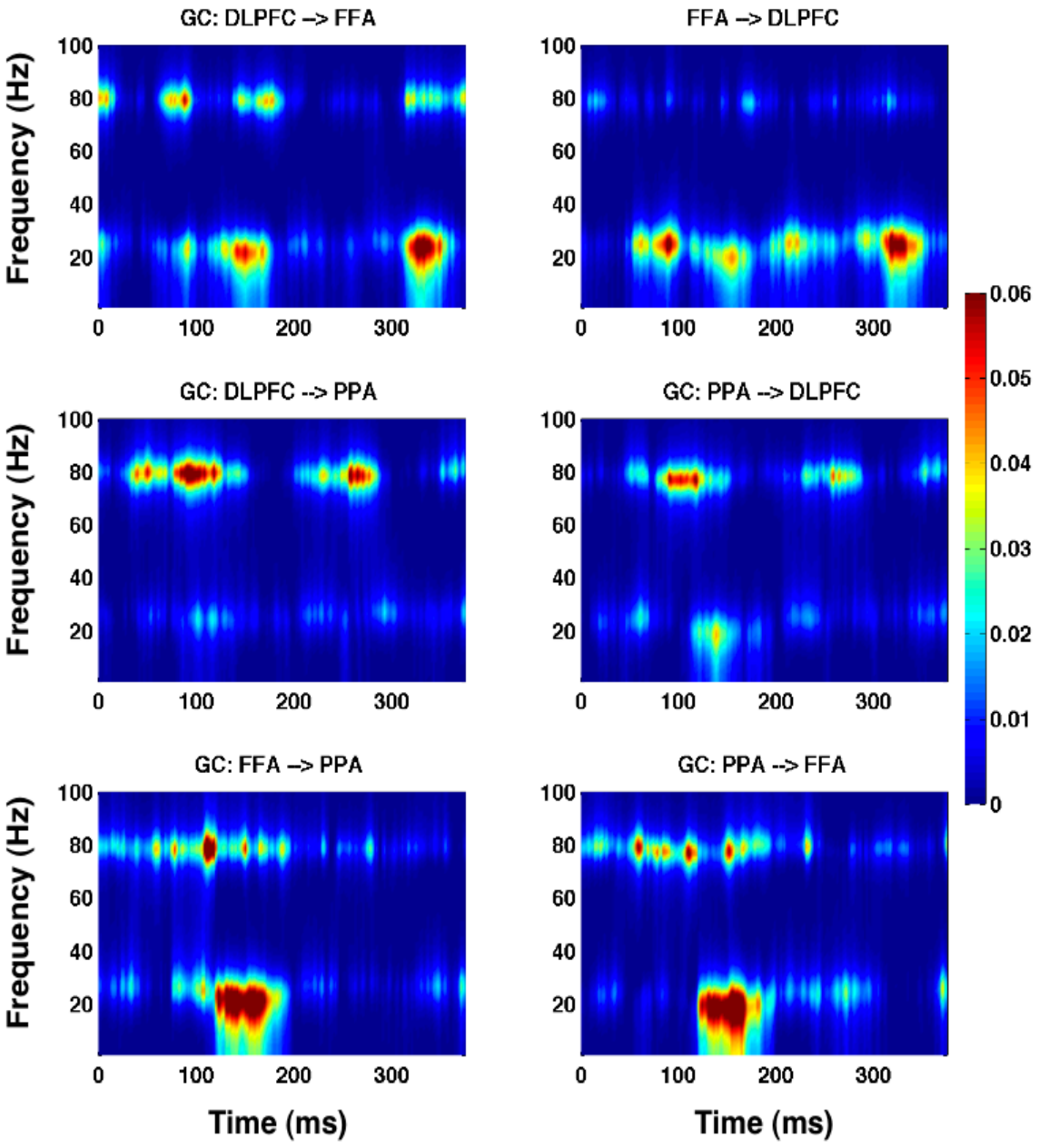

Figure 3.15 Granger causality spectra among the VTC-DLPFC nodes as a function of time and frequency for stimuli with 0% noise.

Granger causality (GC) spectra as a function of entire time window (sliding time in milliseconds) and frequency for stimuli with 0% noise-level illustrating beta and gamma activities. The first row shows GC between DLPFC-FFA pair, second row shows GC between DLPFC-PPA pair, and third row displays GC between FFA-PPA pair.

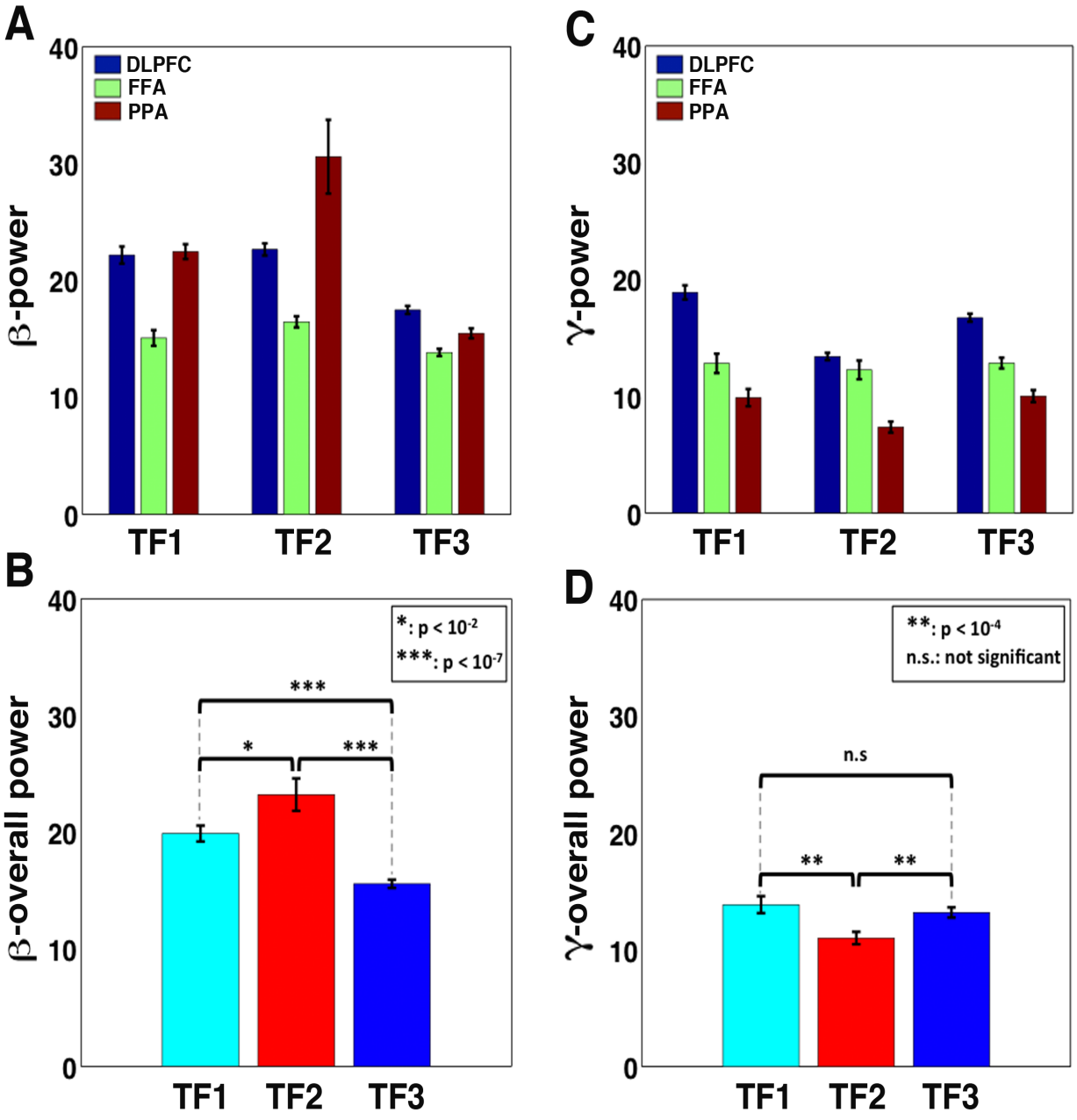

Figure 3.16 Power comparison at the VTC-DLPFC nodes among three consecutive time frames for stimuli with 0% noise.

Power comparison at the DLPFC, FFA, and PPA in three consecutive timeframes (TF1: 0-125 ms, TF2: 125-250 ms, and TF3: 250 ms to 375 ms) for 0% noise-level. Pannels (A, B) show beta power is significantly higher in the TF2 compared to other TFs; and panels (C, D) show gamma power is significantly higher in the TF1 compared to other TFs.

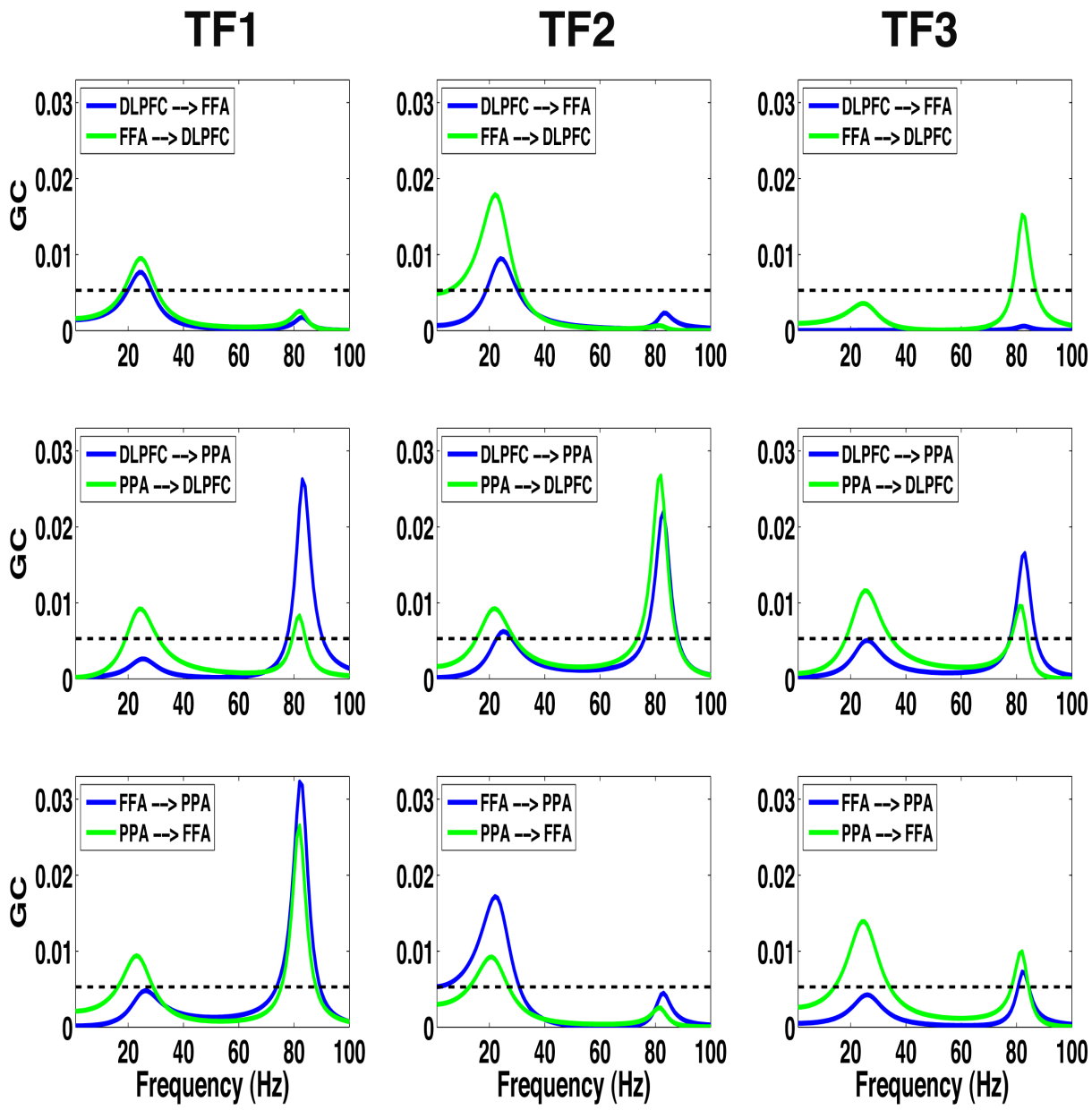

Figure 3.17 Granger causality spectra among the VTC-DLPFC nodes in three consecutive time frames for stimuli with 0% noise.

Granger causality (GC) spectra of all possible pairs among the FFA, PPA, and DLPFC for 0% noise-level in three consecutive timeframes (TF1: 0-125 ms, TF2: 125-250 ms, and TF3: 250-375 ms mentioned at the top of each column) showing beta and gamma oscillations.

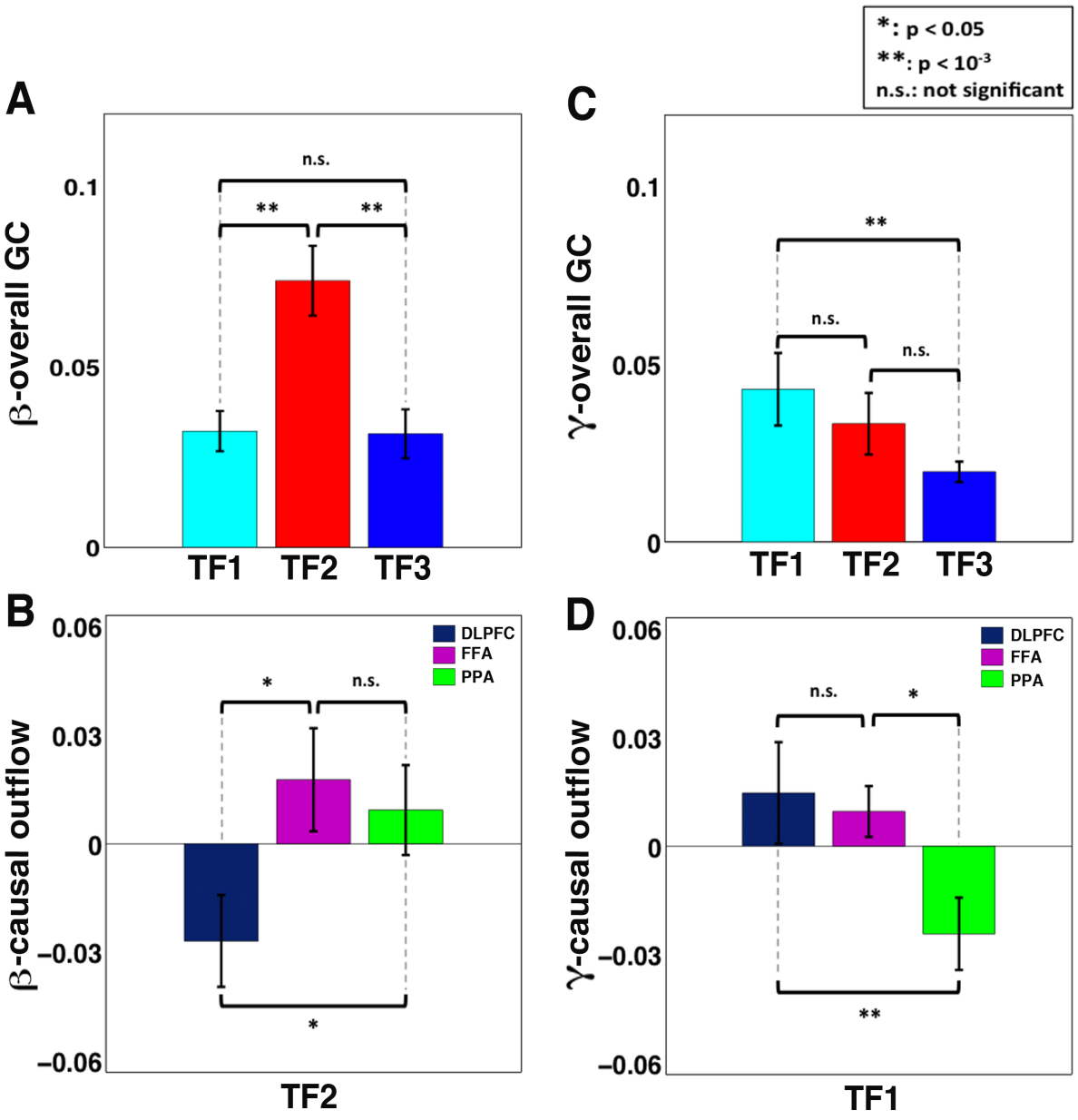

Figure 3.18 Comparison of overall Granger causality among three consecutive time frames and calculation of net outflow for stimuli with 0% noise.

Overall Granger causality (GC) strengths among all possible pairs of the FFA, PPA, and DLPFC among three consecutive timeframes (TF1: 0-125 ms, TF2: 125-250 ms, and TF3: 250-375 ms) for 0% noise-level in beta band (panel A) and in gamma band (panel C). Net GC outflow computed at TF2 (highest activity time frame) in beta band (panel B) shows VTC (FFA and PPA) as outflow hubs, and net GC outflow computed at TF1 (highest activity time frame) in gamma band (D) shows the DLPFC as a main outflow hub within the network.

Figure 3.17 shows GC spectra as a function of frequency, where horizontal lines represent statistically significant threshold value. Beta band network interactions among these nodes are enhanced in TF2 relative to the other TFs (other columns). The overall connectivity strength between these nodes was significantly higher in TF2 compared to other TFs (Figure 3.18A). Net outflow calculations at each node in TF2 (time frame of highest activity in terms of power and connectivity) showed that the FFA and PPA as the main outflow hubs and the DLPFC as a main inflow hub in the network (Figure 3.18B). In the gamma band, network interactions were enhanced in TF1 over the other TFs (other columns). The overall connectivity strength among these nodes was significantly higher in TF1 compared to other TFs (Figure 3.18C). Net outflow calculations at each node in TF1 (time frame of highest activity in terms of power and connectivity) showed the DLPFC as a main outflow hub in the network (Figure 3.18D).

Power spectra were also computed in TF1, TF2 and TF3 at the DLPFC, FFA and PPA when participants perceived the stimuli with 40% and 55% noise-levels. Power spectra calculations also showed peak activity in beta band and gamma band. Both beta and gamma overall powers were significantly enhanced with task-difficulty in their respective highest activity timeframe (Figure 3.19). GC spectra were computed to assess the neural network interactions among these nodes.

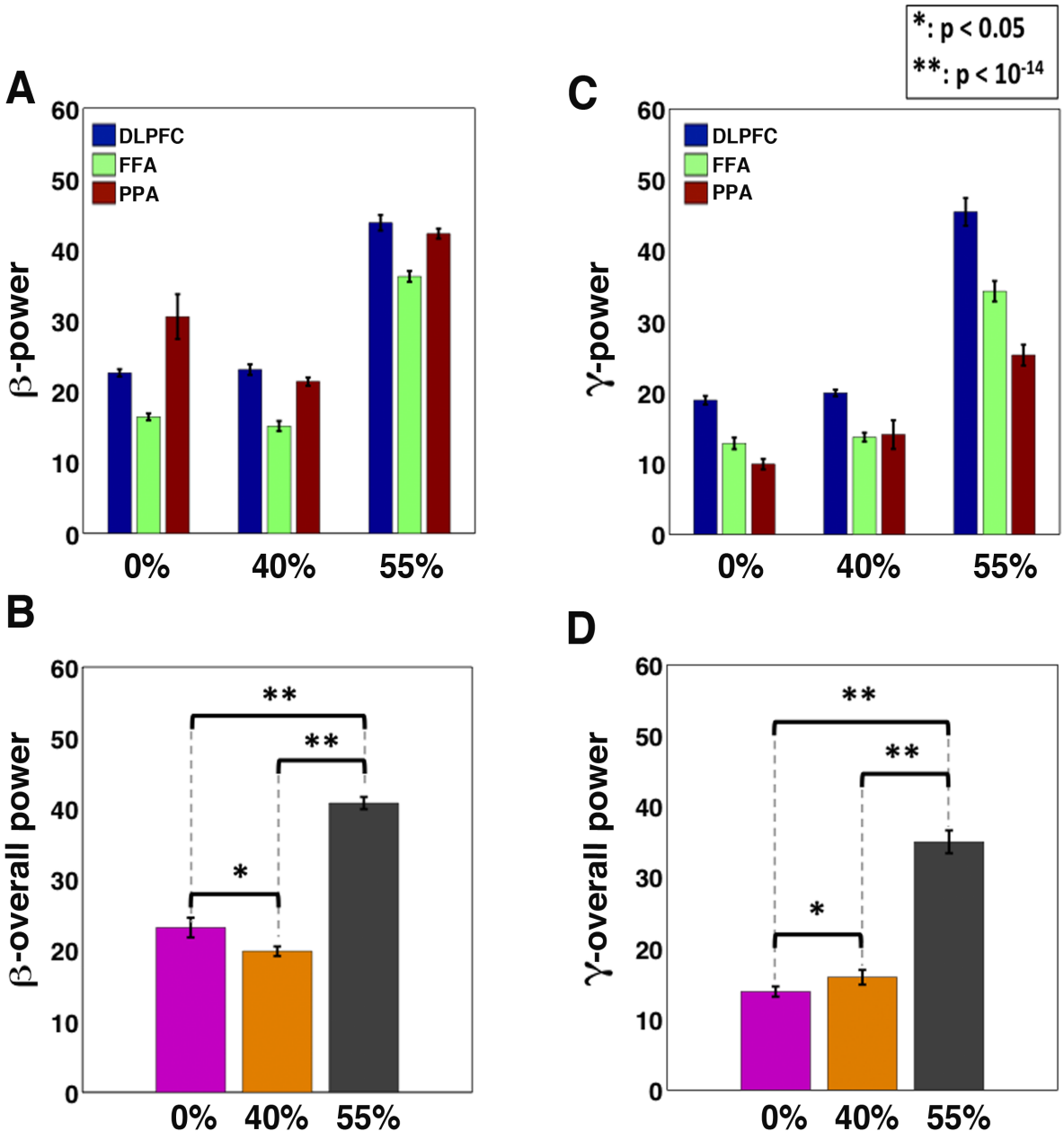

Figure 3.19 Power comparison at the VTC-DLPFC nodes among all three-noise levels.

Power at the DLPFC, FFA, and PPA among all three noise levels: in the TF2 (125-250 ms) for beta band (A, B), and in the TF1 (0-125ms) for gamma band (C, D) (p indicates statistically significant difference).

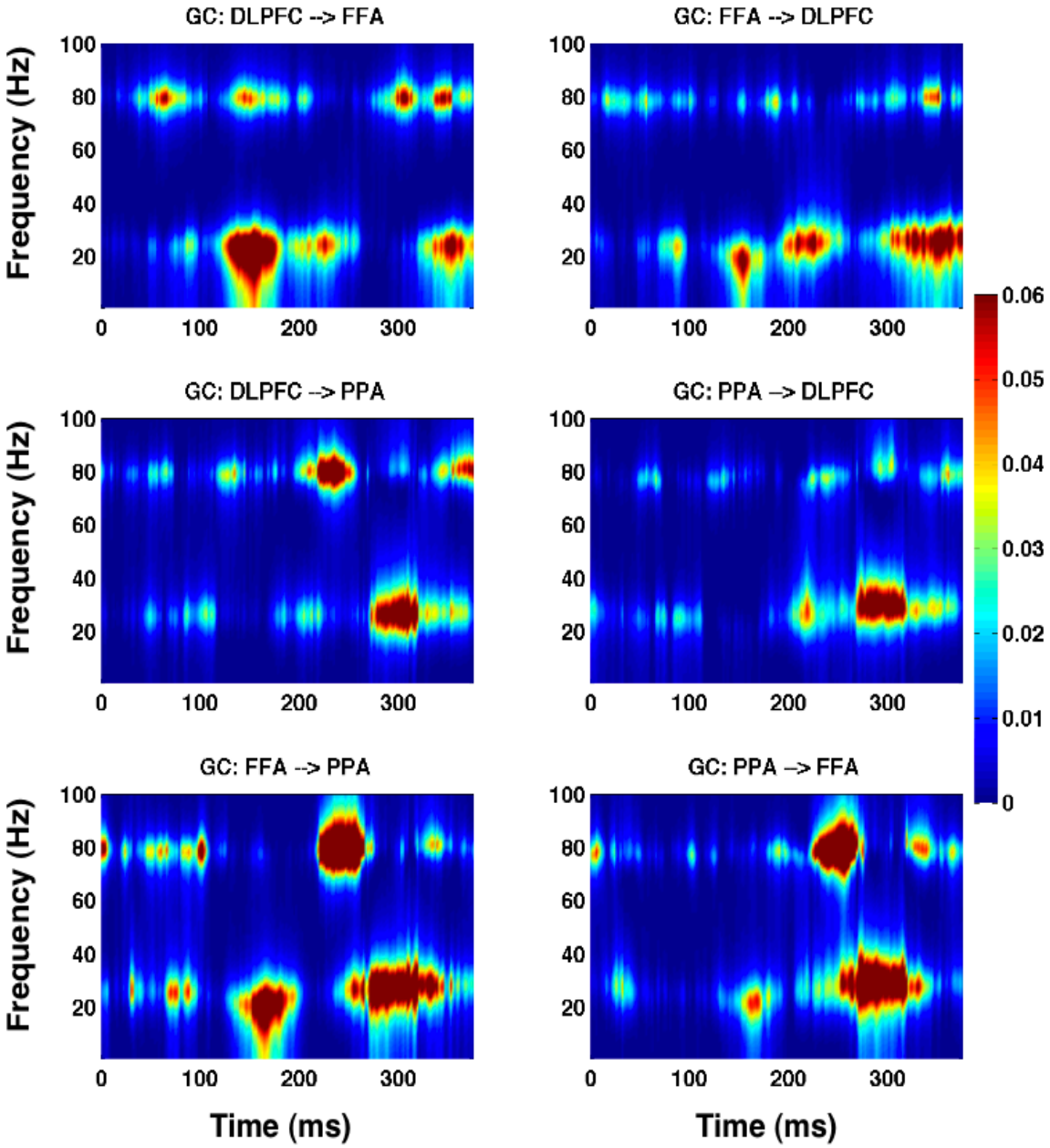

Figure 3.20 Granger causality spectra among the VTC-DLPFC nodes as a function of time and frequency for stimuli with 40% noise.

Granger causality (GC) spectra as a function of entire time window (sliding time in milliseconds) and frequency for stimuli with 40% noise-level illustrating beta and gamma activities. The first row shows GC between DLPFC-FFA pair, second row shows GC between DLPFC-PPA pair, and third row displays GC between FFA-PPA pair.

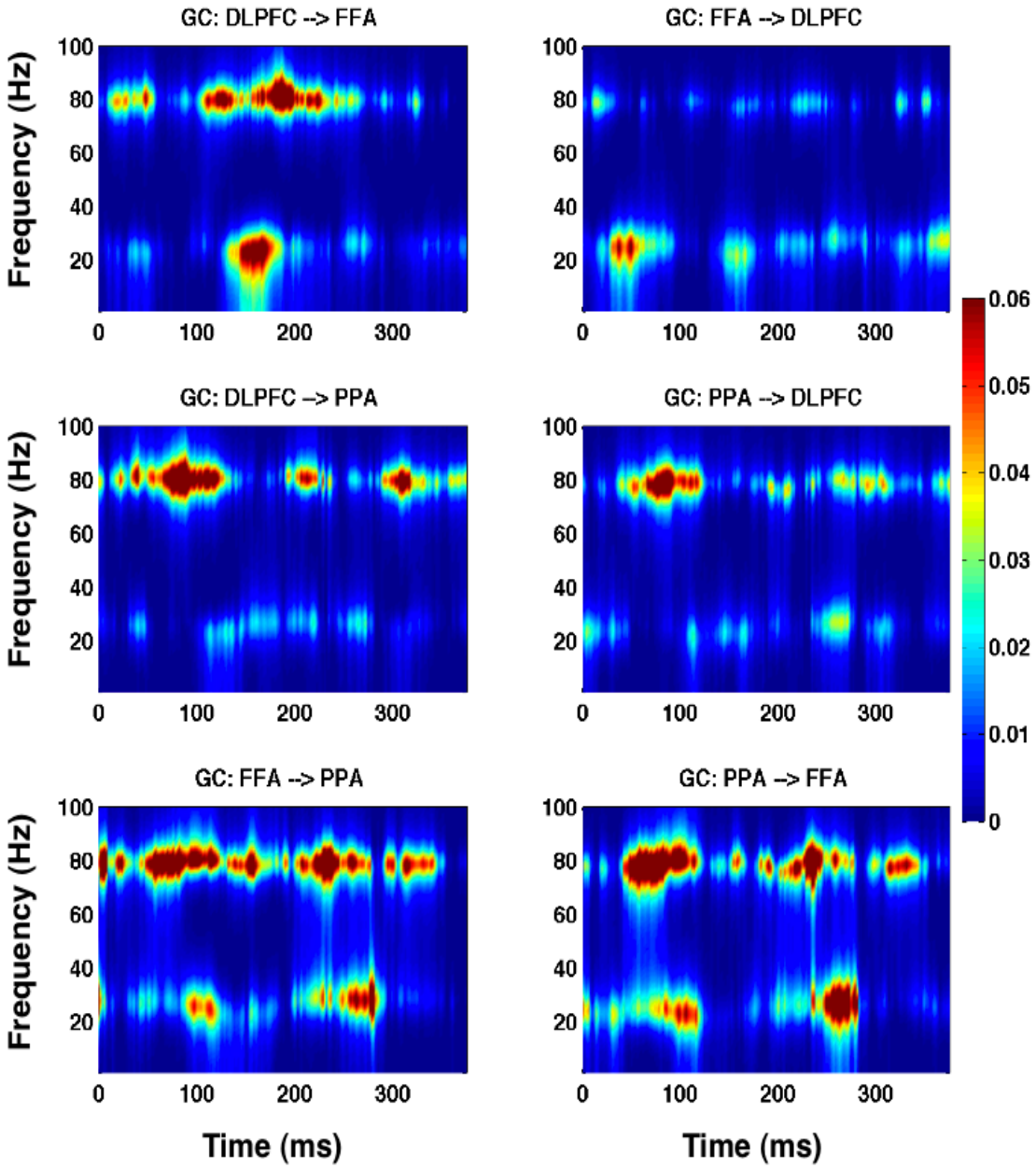

Figure 3.21 Granger causality spectra among the VTC-DLPFC nodes as a function of time and frequency for stimuli with 55% noise.
Granger causality (GC) spectra as a function of entire time window (sliding time in milliseconds) and frequency for stimuli with 55% noise-level illustrating beta and gamma activities. The first row shows GC between DLPFC-FFA pair, second row shows GC between DLPFC-PPA pair, and third row displays GC between FFA-PPA pair.

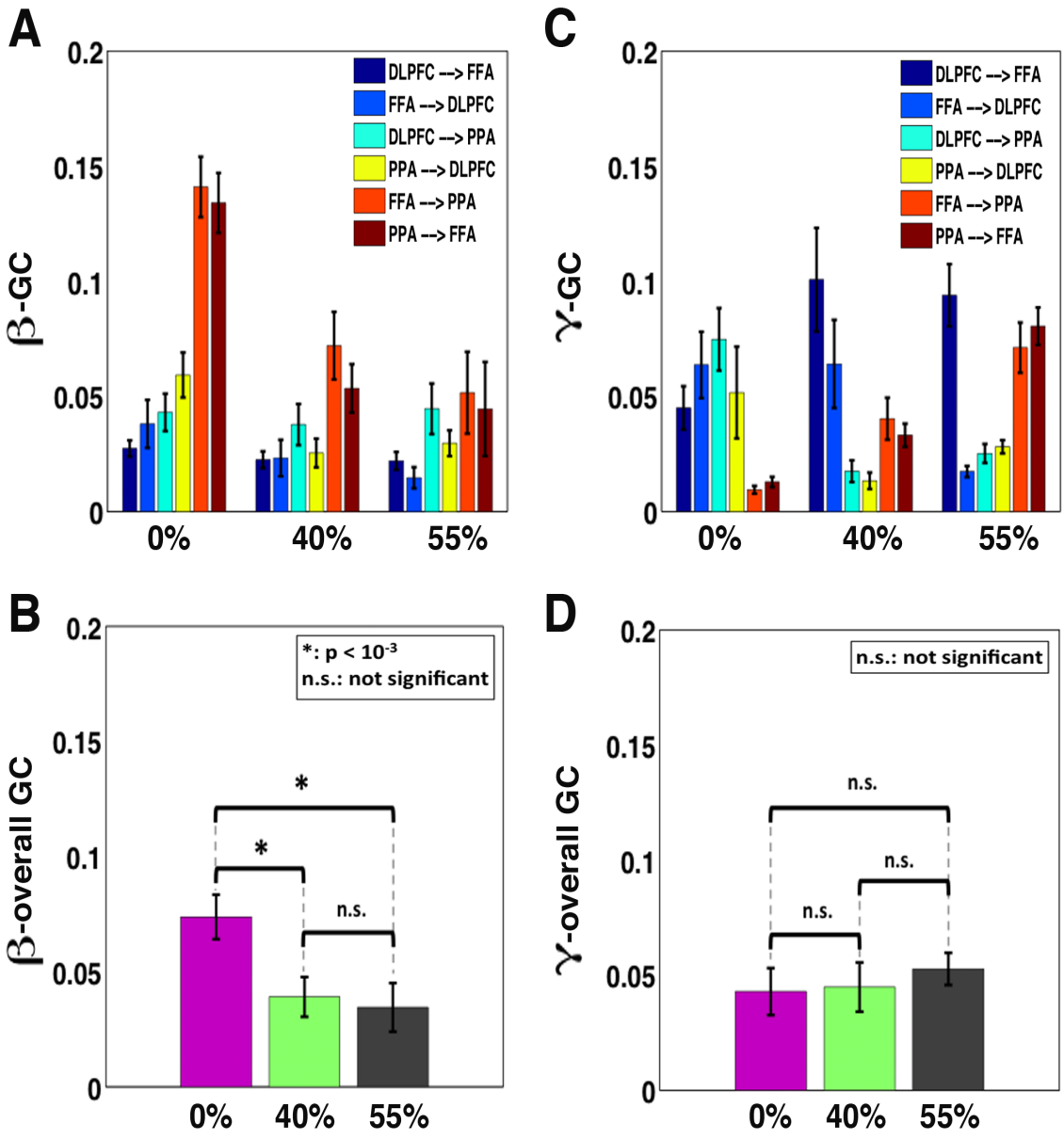

Figure 3.22 Comparison of Granger causality strengths among the VTC-DLPFC nodes among all three-noise levels.
Comparison of Granger causality (GC) connectivity strengths among the FFA, PPA, and DLPFC among all three noise levels: in the TF2 (125-250 ms) for beta band (A, B), and in the TF1 (0-125ms) for gamma band (C, D).

We computed GC spectra using a sliding window (Figure 3.20 and Figure 3.21) to see the activity in entire time for 40% and 55% noise-levels. To further assess how

GC spectra change over time, we then performed calculations at three time frames. Beta overall network interactions among these nodes were compared between the three noise-levels in TF2 by paired t-test to assess the significant effect of task difficulty. We found that beta overall information flow was significantly suppressed when the noise-level was elevated from 0% to 40%. Overall causal interactions among these nodes were further showed decreasing patterns when the noise-level was elevated from 40% to 55% (Figure 3.22). One the other hand, gamma overall information flow showed increasing patterns, specifically a more enhanced feature between the FFA and the PPA (Figure 3.22 C), with the increase in noise level of the stimuli in TF1.

In beta band, we uncovered that the response time (or the difficulty level) was negatively correlated with the measures of network activity for all possible connections between the DLPFC, FFA and PPA in TF2. In gamma band, the response time (or the difficulty level) was positively correlated with the measures of network activity, especially in the FFA-PPA pair, in TF1. The correlation coefficient (r) and the corresponding p-value of all possible connections are presented in Figures 3.23, 3.24.

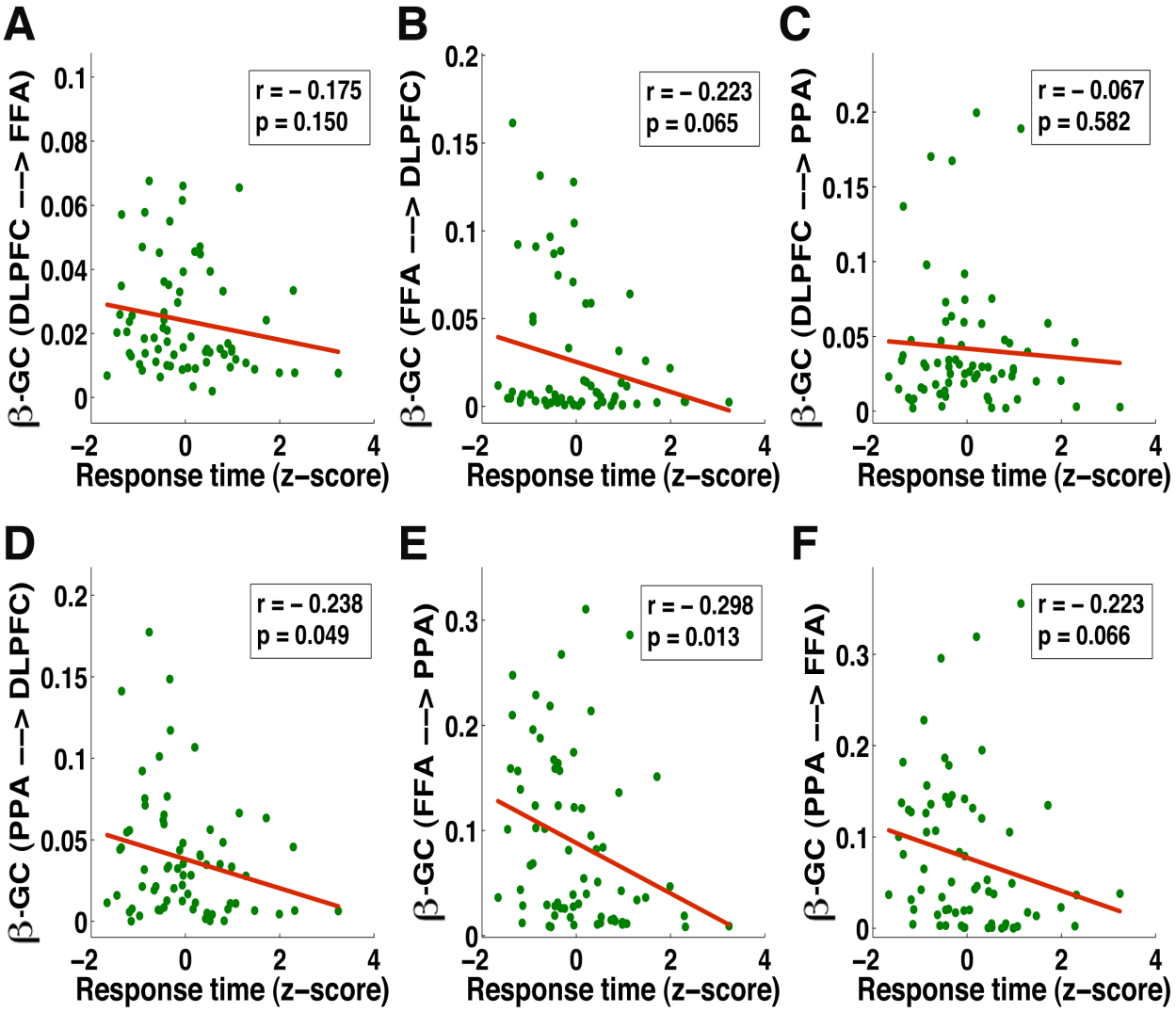

Figure 3.23 Relation between Granger causality and response time in beta band. Granger causality (GC) decreased with difficulty level of tasks, expressed in terms of response time for all three noise-levels, in TF2: 125-250 ms in beta band (r represents correlation coefficient and $p < 0.05$ represents statistically significant correlation).

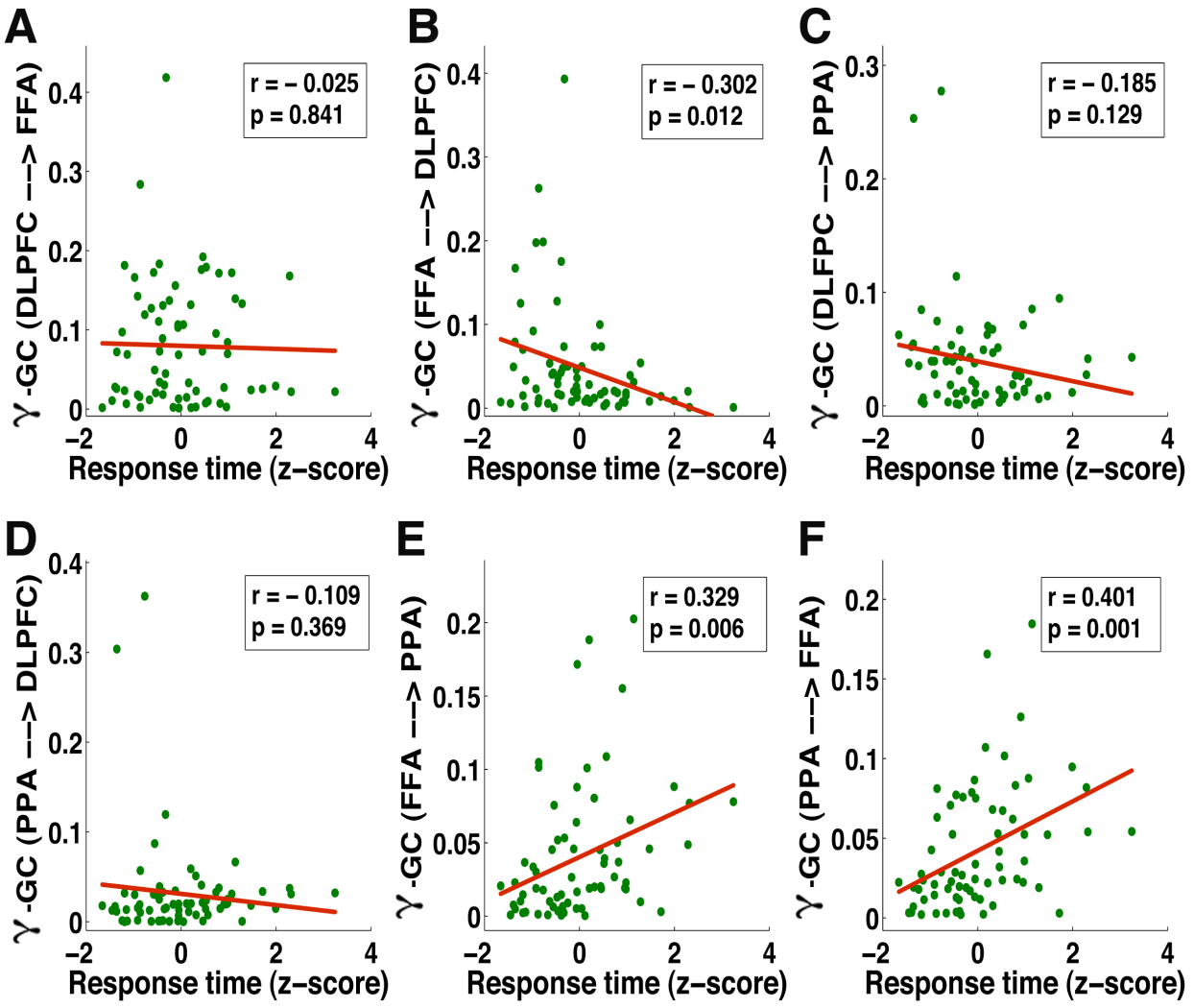

Figure 3.24 Relation between Granger causality and response time in gamma band. Granger causality (GC) increased with difficulty level of tasks (expressed in terms of response time for all three noise-levels), especially in FFA-PPA pair (E, F), in TF1: 0-125 ms in gamma band (r represents correlation coefficient and $p < 0.05$ represents statistically significant correlation).

3.4 Discussion

3.4.1 Salience network dynamics

Behaviorally important events are responsible to activate the SN (67, 68). The AI and dACC are among the most frequently activated brain areas in a wide range of functional neuroimaging studies (143-146) and they also exhibit strong functional covariance across tasks

(66, 144, 147-149). As the SN nodes—the rAI, lAI and dACC—are often co-activated in fMRI BOLD responses (69, 150) it is therefore difficult to clearly identify their distinct functional roles within a network. In this study, using EEG recordings and perceptual decision-related reconstructed EEG sources, we looked at the temporal changes of network activity flow within SN. Using spectral GC analyses, we found that beta oscillation bound these nodes in the SN. The beta power and beta causal interactions were significantly higher at the nodes and network in the time frame 75-150 ms compared to other time frames. The analysis of the net beta causal outflow (out – in causality) patterns showed that the rAI acted as a main cortical outflow hub of the SN consistent with previous fMRI studies of the SN (69, 90). We also found that the beta causal interactions within the SN were significantly suppressed with the task difficulty (noise level). The causal outflow was negatively correlated with the response time.

We found that the key nodes of SN—the rAI, lAI and dACC—activated at around 100 ms after stimulus onset. These brain regions have been demonstrated as also being activated for a variety of tasks in previous fMRI investigations (67-69). Electrophysiological recordings combined with source localization techniques (113, 151) reported that the dACC responds to salient events, such as error detection, in the time frame of 80-110 ms. The timing of dominant activation of the dACC in our study was consistent with those studies. Similarly, the AI was reported as being activated at ~60 ms after stimulus onset, however it was in a thermo-sensory domain (152). Previous study on monkeys had found that the AI activated at ~65 ms after stimulus onset, however it was in an auditory domain (153). Timings of activations demonstrated in our study were not only close in line with previous studies that considered either AI or dACC, but also resolved the overall time frame of activations that appeared in rAI, lAI and dACC.

Power spectra estimated at the rAI, lAI and dACC showed prominent peak

activity in the beta band when the participants viewed clear stimuli. Beta oscillations were also at work for noisy stimuli. Studies have traditionally reported the association of beta oscillations with motor functions (20-24). Beta band that we found was consistent with ones observed in previous EEG studies of multisensory (25) and somatosensory (120) perceptions. The role of beta oscillations is shown in maintaining better accuracy of the task such as during decision-making (25, 26).

GC spectral analyses demonstrated that inter-areal brain synchronization and interactions within the SN are mediated by enhanced beta band neural oscillations. Information flow in the beta band was dominantly feedforward from the rAI and lAI to the dACC, similar to the propagation of average cortical activity, probably reflecting sensory-driven processes. This supports the model of feedforward hierarchical integration process from sensation to those ultimately ends up into action (154, 155). Previous investigations that consider nodes of the SN have divided into two competing groups. One group supports that activity in the dACC implies an enhanced cognitive control (88), and further interactions of the dACC with the lateral prefrontal structures implement subsequent behavioral changes (88, 89). Prior studies suggest its direct role (156) in response or action selection and conflict monitoring (156, 157). Electrophysiological studies (113, 151) suggested that the dACC provides the first cortical signal used for salient events, such as error detection. Other studies support that the rAI drives the SN, partly because the rAI is shown to be structurally and functionally connected to a wide range of cortical regions involved in various aspects of cognitive control. The rAI is functionally connected to networks responsible for adaptive behavior, including the SN (67), as well as other parts of the fronto-parietal control network (158). DTI tractography has demonstrated that this cortical area has direct white matter connections to other key regions within these networks,

including the dACC (159), the inferior parietal lobe (160), and the temporo-parietal junction (161) making the insula well placed to perform its putative role of evaluating (160), reorienting attention (150, 162), and switching between cognitive resources in response to salient events (163). In addition to its role in external inputs, the insula is reported to be sensitive to internal autonomic signals such as heartbeat, skin conductance, and respiration (164, 165) making it a possible hub for interceptive awareness of salient events (66). In the human brain, the AI and dACC also share unique features at cellular level. These brain regions contain a special type of neuron, so called Von Economo neurons (VENs), which have wider axons and are believed to provide rapid relay of control signals from the AI and dACC to the other parts of the brain (166-169). While there is an ongoing division based on previous studies, our results demonstrate that the rAI is a main 'cortical outflow hub' and the dACC is a main 'cortical inflow hub' of the SN. As cortical circuits implementing cognitive processes might engage in highly recurrent interactions (170) mediated by bidirectional cortico-cortical connections (171), our results also demonstrate that beta networks are bidirectional such as in rAI-lAI pair, however a dominant flow is from the rAI to lAI in the time frame of highest activity. With an elevated difficulty level, overall connectivity strengths were significantly suppressed in beta networks. This suppression might be due to less information flow from the sensory regions to the dACC when stimuli were degraded. Since beta oscillations have recently been observed for a better performance (or, accuracy) during decision-making processes (25, 26, 172), this suppressed information flow might implicate the underlying neuronal mechanisms of the SN that has also been behaviorally reflected for an elevated difficulty level. The anatomical inter-areal and laminar neural circuitry in the brain might support the occurrence of such oscillatory activities and their modulations in cognitive tasks (27).

To summarize, the present study enhances our understanding of the SN, with regards to the temporal evolution of averaged evoked potentials in the nodes and an oscillatory network that appear to organize evoked activity across the SN. We found that the SN became most active at around 100 ms after the stimulus onset; the beta-band (13–30 Hz) oscillations bound them in a network and the rAI acted as a main outflow hub within SN. The SN activity was negatively correlated with the decision response time (decision difficulty). These findings provide important insights about how sensory information enters and organizes in the SN before reaching the prefrontal cortex for decision-makings.

3.4.2 VTC-DLPFC network dynamics

The present study examined the neural oscillatory networks and their dynamics involved during PDM for clear visual stimuli (faces and houses) and their degraded ones. The key nodes of the network involved in visual processing—the FFA, PPA and DLPFC—often co-activate, therefore making it difficult to clearly identify their distinct functional roles within a network, specifically using larger time-scale (seconds) measures such as BOLD-fMRI. Here we resolved the overall temporal flow of activation (in milliseconds) in the FFA, PPA and DLPFC by source localization of EEG recordings. Using GC analyses, we found two distinct oscillatory networks—beta band and gamma band—and their temporal dynamics. First, we demonstrated that beta power and beta causal interactions at the nodes and the network were significantly higher in the 125-250 ms timeframe, the FFA and PPA played as the main outflow hubs and the DLPFC as a main inflow hub in the network, and network interactions were negatively correlated with task-difficulty. Second, gamma power and gamma causal interactions at the nodes and network were significantly higher in the 0-125 ms timeframe, the DLPFC worked as an outflow hub in the network, and network interactions (specifically in the FFA-PPA pair) were

positively correlated with task-difficulty.

The earliest peak of cortical activity occurred in the visual cortex (BA17/18) at ~60 ms after stimulus onset, which was in accord with previous findings (173). Peak activation then occurred in the ventral temporal cortex (BA37: the right FFA and the left PPA) at ~160 ms. Activation of the FFA and the PPA for perception of faces-houses were consistent with fMRI and MEG investigations (98, 99, 102, 105, 174). Moreover, activation time frame of the FFA was also similar with prior reports (122, 123). The peak activation observed in the left DLPFC (BA9) at ~224 ms was close in accord with an electrophysiological study that reported activation of the DLPFC at ~170-210 ms (120), however it was in a somatosensory domain. Activation of the DLPFC in decision-making has been repeatedly reported in previous fMRI and EEG studies (1, 47, 95, 118-120). Our findings thus resolved a systematic source-level activation pattern of temporal evolution in the FFA, PPA and DLPFC for visual face/house categorization tasks.

Power spectra at the FFA, PPA and DLPFC showed peak activity in the beta band and gamma band when the participants perceived clear and noisy faces-houses. Prior studies have linked beta oscillations with motor functions (20-24). More recently, beta oscillations are shown in maintaining accuracy of the task in decision-making (25, 26). Gamma oscillations have been demonstrated in a wide range of brain processes, including focused arousal, multisensory and sensorimotor integration, attention, memory formation, and conscious awareness (13, 27-29). These neural oscillatory features reflect distinct aspect of neuronal synchronization similar to that observed in auditory-visual (25) and somatosensory (120) perceptions. GC spectra among the FFA, PPA and DLPFC also demonstrated that inter-areal brain synchronization and interactions were mediated by the beta

band and gamma band in the visual perceptions. The anatomical inter-areal and laminar neural circuitry in the brain might support the occurrence of such oscillatory activities and their modulations in cognitive tasks (27, 172). Anatomical studies have provided the evidence of rich connections of the DLPFC with sensory areas of the brain as summarized in a previous review (175). The DLPFC receives visual, somatosensory and auditory sensory inputs from the occipital, parietal and temporal cortices (176), and its anatomical connection with pre-motor/motor areas supports the motor outputs (177).

Beta band power and beta network activity were significantly higher in the 125-250 ms time frame after stimulus onset, consistent with average source-level peak activities. Causal outflow calculations in this time frame demonstrated that the lower order sensory areas (the FFA and PPA) acted as outflow hubs and the DLPFC as an inflow hub. This was supported by the model of feedforward hierarchical integration process from sensation to those ultimately ends up into action (154, 155). As cortical circuits implementing cognitive processes might engage highly recurrent interactions (170) mediated by bidirectional cortico-cortical connections (171), our results also demonstrate that interactions were bidirectional, such as in the time frame of highest activity (TF2). Overall connectivity strength was significantly suppressed in the beta neural network for elevated noise-level in the stimuli. Beta neuronal oscillation has been reported for a better accuracy during perception-related tasks (25, 26), so the beta network activity suppression in our study might implicate the underlying neural mechanisms of the network that have also been behaviorally reflected for an elevated difficulty level. Such suppression might result due to less flow of decision-related information among the FFA, PPA and DLPFC when the stimuli were degraded.

In contrast, gamma band results (clear stimuli) demonstrated that it was more dominant in

the time frame 0-125 ms compared to the other time frames. Net causal outflow computed in this time frame further demonstrated the DLPFC as an outflow hub. This was in accord with a well-known role of DLPFC in top-down processing for attentional selection of relevant sensory information and sensory updating (175). We provided this direct evidence from temporal dynamics of gamma oscillatory network activity. Gamma oscillations have been consistently reported for perceptual binding (15, 178) for a variety of tasks. Enhanced features of the node and the network activity - more prominent effects in a FFA-PPA pair in the network - with task-difficulty might imply that such bindings are required for behaviorally harder decisions/tasks.

In summary, we evaluated the timing and oscillatory networks dynamics involved in the key nodes - the FFA, PPA and DLPFC - of faces-houses perceptions. We demonstrated that the beta band network was most active in 125-250 ms, the FFA and PPA acted as main outflow hubs, and the beta network was negatively correlated with the decision response time (task difficulty). We further found that the gamma band network was most active in 0-125 ms, the DLPFC acted as a main outflow hub, and the gamma network was positively correlated with the decision response time. These findings provide us with important insights about how sensory information enters and organizes in the FFA, PPA and DLPFC during visual perceptual decision-making.

4 SUMMARY AND FUTURE STUDIES

The present study investigated large-scale neuronal oscillations captured by scalp electroencephalography in perceptual decision-making. We used clear and noisy face/house image categorization tasks, applied source reconstruction technique, found the nodes of two distinct networks, and evaluated directed connectivity analyses among brain areas within each network using Granger causality.

Prior studies on the salience network have often relied on the sluggish response of BOLD-fMRI. Those studies report that the salience network supports cognitive functions, including communication, social behavior, and sensory stimulus-guided goal-directed behaviors (61, 66, 70-72, 179). Recent findings have shown that the SN is atypically engaged in several neuropsychiatric disorders, such as in autism spectrum disorder (73-77), schizophrenia (78-83), and frontotemporal dementia (84-87). Despite extensive studies, how sensory information enters and organizes within this network was poorly known. Our study in finer time-scale demonstrated that the beta oscillations mediated the activity in salience nodes and network, became most active around 100 ms after the stimulus onset, and the rAI acted as a main outflow hub within network. The Granger causality strengths correlated negatively with the difficult tasks (decision response times) within the nodes of the salience network. These findings help to better understand when and how a sensory signal enters and organizes within the salience network before reaching the central executive network including the prefrontal cortex.

Studies that recorded BOLD-fMRI signals have also suggested that the VTC (FFA and PPA) and DLPFC coordinate in a network to categorize a face or a house (1, 47, 119). How sensory signal enters and organizes within the VTC-DLPFC during decision-making is not well understood. We evaluated the VTC-DLPFC network in finer time-scale during perceptual decision-making task. We uncovered that the VTC-DLPFC network activities were mediated by beta and gamma oscillations. Beta activities significantly enhanced in the time frame 125-250 ms after stimulus onset, and the VTC (FFA and PPA) acted as the main outflow hub within the VTC-DLPFC network. The Granger causality strengths correlated negatively with the difficult tasks (decision response times) within the nodes of VTC-DLPFC network. In contrast, gamma activities significantly elevated in the time frame 0-125 ms, and the DLPFC played as a main

outflow hub, and Granger causality network activities—specifically the FFA-PPA pair—correlated positively with the difficult tasks (decision response times). These results significantly enhance our understanding of when and how sensory information enters and organizes within the VTC-DLPFC network for visual perception. We thus investigated the dynamics of two distinct neurocognitive networks in perceptual decision-making task in milliseconds time-scale. To our knowledge, there are no studies that report how sensory signals enter and organize within these networks on the millisecond time-scale of human perception and decision-making.

Future studies should direct towards resolving the milliseconds temporal dynamics of each network in the brain—there are other networks besides these two—and then elucidating the information flow patterns among those networks, such as how information flow pattern alters in millisecond time segments. One potential challenge that we need to be aware of is the selection of time frames if the nodes are activated at very distinct and widely separated times. Studies have begun to examine a unified network approach (multiple networks interactions) (90, 179, 180), at least for larger time-scale measures. We believe that our findings will encourage further investigation of the interactions within and between networks in a millisecond time-scale.

REFERENCES

1. H. R. Heekeren, S. Marrett, L. G. Ungerleider, The neural systems that mediate human perceptual decision making. *Nature reviews. Neuroscience* **9**, 467 (2008).
2. M. Siegel, T. J. Buschman, E. K. Miller, Cortical information flow during flexible sensorimotor decisions. *Science* **348**, 1352 (2015).
3. M. G. Philiastides, R. Auksztulewicz, H. R. Heekeren, F. Blankenburg, Causal role of dorsolateral prefrontal cortex in human perceptual decision making. *Current biology : CB* **21**, 980 (2011).
4. G. B. Chand, M. Dhamala, Spectral factorization-based current source density analysis of ongoing neural oscillations. *Journal of neuroscience methods* **224**, 58 (2014).
5. G. Buzsaki, Rhythms of the brain. *Oxford University Press*, (2006).
6. S. L. Bressler, Large-scale cortical networks and cognition. *Brain Research Reviews* **20(3)**, 288 (1995).
7. P. L. Nunez, R. Srinivasan, Electric fields of the brain: the neurophysics of EEG. *Oxford University Press* **Second edition**, (2006).
8. H. Berger, *Eur Arch Psychiatry Clin Neurosci* **87**, (1929).
9. M. Moazami-Goudarzi, L. Michels, N. Weisz, D. Jeanmonod, Temporo-insular enhancement of EEG low and high frequencies in patients with chronic tinnitus. QEEG study of chronic tinnitus patients. *BMC neuroscience* **11**, 40 (2010).
10. S. Velikova *et al.*, Dysfunctional brain circuitry in obsessive-compulsive disorder: source and coherence analysis of EEG rhythms. *NeuroImage* **49**, 977 (2010).

11. A. K. Engel, P. Fries, Beta-band oscillations--signalling the status quo? *Current opinion in neurobiology* **20**, 156 (2010).

12. G. G. Knyazev, Motivation, emotion, and their inhibitory control mirrored in brain oscillations. *Neuroscience and biobehavioral reviews* **31**, 377 (2007).

13. P. Fries, Neuronal gamma-band synchronization as a fundamental process in cortical computation. *Annual review of neuroscience* **32**, 209 (2009).

14. A. C. Etchell, B. W. Johnson, P. F. Sowman, Beta oscillations, timing, and stuttering. *Frontiers in human neuroscience* **8**, 1036 (2014).

15. P. J. Uhlhaas, C. Haenschel, D. Nikolic, W. Singer, The role of oscillations and synchrony in cortical networks and their putative relevance for the pathophysiology of schizophrenia. *Schizophrenia bulletin* **34**, 927 (2008).

16. G. Buzsaki, A. Draguhn, Neuronal oscillations in cortical networks. *Science* **304**, 1926 (2004).

17. J. F. Burke *et al.*, Synchronous and asynchronous theta and gamma activity during episodic memory formation. *The Journal of neuroscience : the official journal of the Society for Neuroscience* **33**, 292 (2013).

18. O. Jensen, J. E. Lisman, Hippocampal sequence-encoding driven by a cortical multi-item working memory buffer. *Trends in neurosciences* **28**, 67 (2005).

19. S. Palva, J. M. Palva, New vistas for alpha-frequency band oscillations. *Trends in neurosciences* **30**, 150 (2007).

20. S. N. Baker, Oscillatory interactions between sensorimotor cortex and the periphery. *Current opinion in neurobiology* **17**, 649 (2007).

21. C. N. Riddle, S. N. Baker, Digit displacement, not object compliance, underlies task dependent modulations in human corticomuscular coherence. *NeuroImage* **33**, 618 (2006).

22. V. Chakarov *et al.*, Beta-range EEG-EMG coherence with isometric compensation for increasing modulated low-level forces. *Journal of neurophysiology* **102**, 1115 (2009).

23. F. Klostermann *et al.*, Task-related differential dynamics of EEG alpha- and beta-band synchronization in cortico-basal motor structures. *The European journal of neuroscience* **25**, 1604 (2007).

24. N. J. Davis, S. P. Tomlinson, H. M. Morgan, The role of beta-frequency neural oscillations in motor control. *The Journal of neuroscience : the official journal of the Society for Neuroscience* **32**, 403 (2012).

25. J. F. Hipp, A. K. Engel, M. Siegel, Oscillatory synchronization in large-scale cortical networks predicts perception. *Neuron* **69**, 387 (2011).

26. M. Siegel, A. K. Engel, T. H. Donner, Cortical network dynamics of perceptual decision-making in the human brain. *Frontiers in human neuroscience* **5**, 21 (2011).

27. G. Buzsaki, X. J. Wang, Mechanisms of gamma oscillations. *Annual review of neuroscience* **35**, 203 (2012).

28. O. Jensen, J. Kaiser, J. P. Lachaux, Human gamma-frequency oscillations associated with attention and memory. *Trends in neurosciences* **30**, 317 (2007).

29. D. Senkowski, T. R. Schneider, J. J. Foxe, A. K. Engel, Crossmodal binding through neural coherence: implications for multisensory processing. *Trends in neurosciences* **31**, 401 (2008).

30. A. Schnitzler, J. Gross, Normal and pathological oscillatory communication in the brain. *Nature reviews. Neuroscience* **6**, 285 (2005).

31. K. J. Friston, Functional and effective connectivity in neuroimaging: a synthesis. *Human Brain Mapping* **2(1-2)**, 56 (1994).

32. N. Wiener, The theory of prediction. *Modern Mathematics for the Engineers, McGraw-Hill, NY*, 165 (1956).

33. C. Granger, Investigating causal relations by econometric models and cross-spectral methods. *Econometrica: J Econometric Society* **37(3)**, 424 (1969).

34. C. Granger, Testing for causality: a personal viewpoint. *J Econ Dyn Control* **2**, 329 (1980).

35. X. Wen, Y. Liu, L. Yao, M. Ding, Top-down regulation of default mode activity in spatial visual attention. *The Journal of neuroscience : the official journal of the Society for Neuroscience* **33**, 6444 (2013).

36. J. Geweke, Measures of conditional linear-dependence and feedback between time-series. *J Am Stat Assoc* **79**, 907 (1984).

37. B. M. Adhikari, C. M. Epstein, M. Dhamala, Localizing epileptic seizure onsets with Granger causality. *Phys Rev E* **88**, 030701(R) (2013).

38. A. K. Seth, A MATLAB toolbox for Granger causal connectivity analysis *J Neurosci Methods* **186**, 262 (2010).

39. A. Brovelli *et al.*, Beta oscillations in a large-scale sensorimotor cortical network: directional influences revealed by Granger causality. *Proc. Natl. Acad. Sci. U. S. A.* **101**, 9849 (2004).

40. M. Dhamala, G. Rangarajan, M. Ding, Analyzing information flow in brain networks with nonparametric Granger causality. *NeuroImage* **41**, 354 (2008).

41. M. Dhamala, G. Rangarajan, M. Ding, Estimating Granger Causality from Fourier and Wavelet Transforms of Time Series Data. *Phys Rev Lett* **100**, (2008).

42. M. Ding, Y. Chen, S. Bressler, Handbook of Time Series Analysis: Recent Theoretical Developments and Applications. **(Eds.) B. Schelter, M. Winterhadler, J. Timmers**, Wiley (2006).

43. W. T. Newsome, K. H. Britten, J. A. Movshon, Neuronal correlates of a perceptual decision. *Nature* **341**, 52 (1989).

44. J. N. Kim, M. N. Shadlen, Neural correlates of a decision in the dorsolateral prefrontal cortex of the macaque. *Nat. Neurosci.* **2**, 176 (1999).

45. J. I. Gold, M. N. Shadlen, The neural basis of decision making. *Annual review of neuroscience* **30**, 535 (2007).

46. T. D. Hanks *et al.*, Distinct relationships of parietal and prefrontal cortices to evidence accumulation. *Nature* **520**, 220 (2015).

47. H. R. Heekeren, S. Marrett, P. A. Bandettini, L. G. Ungerleider, A general mechanism for perceptual decision-making in the human brain. *Nature* **431**, 859 (2004).

48. T. H. Donner, M. Siegel, P. Fries, A. K. Engel, Buildup of choice-predictive activity in human motor cortex during perceptual decision making. *Current biology : CB* **19**, 1581 (2009).

49. S. J. Thorpe, The speed of categorization in the human visual system. *Neuron* **62**, 168 (2009).

50. R. Ratcliff, M. G. Philiastides, P. Sajda, Quality of evidence for perceptual decision making is indexed by trial-to-trial variability of the EEG. *Proceedings of the National Academy of Sciences of the United States of America* **106**, 6539 (2009).

51. A. Tosoni, G. Galati, G. L. Romani, M. Corbetta, Sensory-motor mechanisms in human parietal cortex underlie arbitrary visual decisions. *Nature neuroscience* **11**, 1446 (2008).

52. R. Bogacz, Optimal decision-making theories: linking neurobiology with behaviour. *Trends in cognitive sciences* **11**, 118 (2007).

53. R. Bogacz, E. Brown, J. Moehlis, P. Holmes, J. D. Cohen, The physics of optimal decision making: a formal analysis of models of performance in two-alternative forced-choice tasks. *Psychological review* **113**, 700 (2006).

54. C. Summerfield, F. P. de Lange, Expectation in perceptual decision making: neural and computational mechanisms. *Nature reviews. Neuroscience* **15**, 745 (2014).

55. J. Palmer, A. C. Huk, M. N. Shadlen, The effect of stimulus strength on the speed and accuracy of a perceptual decision. *Journal of vision* **5**, 376 (2005).

56. M. G. Philiastides, R. Ratcliff, P. Sajda, Neural representation of task difficulty and decision making during perceptual categorization: a timing diagram. *The Journal of neuroscience : the official journal of the Society for Neuroscience* **26**, 8965 (2006).

57. J. V. Haxby, E. A. Hoffman, M. I. Gobbini, The distributed human neural system for face perception. *Trends in cognitive sciences* **4**, 223 (2000).

58. S. L. Fairhall, A. Ishai, Effective connectivity within the distributed cortical network for face perception. *Cerebral cortex* **17**, 2400 (2007).

59. M. E. Goldberg, J. W. Bisley, K. D. Powell, J. Gottlieb, Chapter 10 Saccades, salience and attention: the role of the lateral intraparietal area in visual behavior. **155**, 157 (2006).

60. S. Puglisi-Allegra, R. Ventura, Prefrontal/accumbal catecholamine system processes high motivational salience. *Frontiers in behavioral neuroscience* **6**, 31 (2012).

61. L. Q. Uddin, Salience processing and insular cortical function and dysfunction. *Nature reviews. Neuroscience* **16**, 55 (2015).

62. S. Yantis, A. P. Hillstrom, Stimulus-driven attentional capture: evidence from equiluminant visual objects. *J Exp. Psychol. Hum. Percept. Perform.* **20**, 95 (1994).

63. N. Goulden *et al.*, The salience network is responsible for switching between the default mode network and the central executive network: replication from DCM. *Neuroimage* **99**, 180 (2014).

64. E. I. Knudsen, Fundamental components of attention. *Annual review of neuroscience* **30**, 57 (2007).

65. J. H. Fecteau, A. H. Bell, D. P. Munoz, Neural correlates of the automatic and goal-driven biases in orienting spatial attention. *J Neurophysiol* **92**, 1728 (2004).

66. V. Menon, Salience Network. *Brain Mapping: An Enclopedic Reference* 597 (2015).

67. W. W. Seeley *et al.*, Dissociable intrinsic connectivity networks for salience processing and executive control. *J Neurosci* **27**, 2349 (2007).

68. V. Menon, L. Q. Uddin, Saliency, switching, attention and control: a network model of insula function. *Brain structure & function* **214**, 655 (2010).

69. T. Ham, A. Leff, X. de Boissezon, A. Joffe, D. J. Sharp, Cognitive control and the salience network: an investigation of error processing and effective connectivity. *The Journal of neuroscience : the official journal of the Society for Neuroscience* **33**, 7091 (2013).

70. N. Gogolla, A. E. Takesian, G. Feng, M. Fagiolini, T. K. Hensch, Sensory integration in mouse insular cortex reflects GABA circuit maturation. *Neuron* **83**, 894 (2014).

71. A. D. Craig, How do you feel-now? The anterior insula and human awareness. *Nature reviews. Neuroscience* **10**, 59 (2009).

72. E. J. Ploran *et al.*, Evidence accumulation and the moment of recognition: dissociating perceptual recognition processes using fMRI. *The Journal of neuroscience : the official journal of the Society for Neuroscience* **27**, 11912 (2007).

73. D. P. Dickstein *et al.*, Developmental meta-analysis of the functional neural correlates of autism spectrum disorders. *Journal of the American Academy of Child and Adolescent Psychiatry* **52**, 279 (2013).

74. L. Q. Uddin, K. Supekar, V. Menon, Reconceptualizing functional brain connectivity in autism from a developmental perspective. *Frontiers in human neuroscience* **7**, 458 (2013).

75. L. Q. Uddin *et al.*, Salience network-based classification and prediction of symptom severity in children with autism. *JAMA psychiatry* **70**, 869 (2013).

76. A. Di Martino *et al.*, Functional brain correlates of social and nonsocial processes in autism spectrum disorders: an activation likelihood estimation meta-analysis. *Biological psychiatry* **65**, 63 (2009).

77. A. Di Martino *et al.*, The autism brain imaging data exchange: towards a large-scale evaluation of the intrinsic brain architecture in autism. *Molecular psychiatry* **19**, 659 (2014).

78. D. C. Glahn *et al.*, Meta-analysis of gray matter anomalies in schizophrenia: application of anatomic likelihood estimation and network analysis. *Biological psychiatry* **64**, 774 (2008).

79. A. Fornito, M. Yucel, J. Patti, S. J. Wood, C. Pantelis, Mapping grey matter reductions in schizophrenia: an anatomical likelihood estimation analysis of voxel-based morphometry studies. *Schizophrenia research* **108**, 104 (2009).

80. A. M. Shepherd, S. L. Matheson, K. R. Laurens, V. J. Carr, M. J. Green, Systematic meta-analysis of insula volume in schizophrenia. *Biological psychiatry* **72**, 775 (2012).

81. L. van der Meer *et al.*, Neural correlates of emotion regulation in patients with schizophrenia and non-affected siblings. *PloS one* **9**, e99667 (2014).

82. K. P. Wylie, J. R. Tregellas, The role of the insula in schizophrenia. *Schizophrenia research* **123**, 93 (2010).

83. X. Wang *et al.*, Disrupted resting-state functional connectivity in minimally treated chronic schizophrenia. *Schizophrenia research* **156**, 150 (2014).

84. E. J. Kim *et al.*, Selective frontoinsular von Economo neuron and fork cell loss in early behavioral variant frontotemporal dementia. *Cerebral cortex* **22**, 251 (2012).

85. W. W. Seeley, Anterior insula degeneration in frontotemporal dementia. *Brain structure & function* **214**, 465 (2010).

86. G. S. Day *et al.*, Salience network resting-state activity: prediction of frontotemporal dementia progression. *JAMA neurology* **70**, 1249 (2013).

87. J. Zhou *et al.*, Divergent network connectivity changes in behavioural variant frontotemporal dementia and Alzheimer's disease. *Brain : a journal of neurology* **133**, 1352 (2010).

88. K. R. Ridderinkhof, M. Ullsperger, E. A. Crone, S. Nieuwenhuis, The role of the medial frontal cortex in cognitive control. *Science* **306**, 443 (2004).

89. T. Egner, Prefrontal cortex and cognitive control: motivating functional hierarchies. *Nature neuroscience* **12**, 821 (2009).

90. D. Sridharan, D. J. Levitin, V. Menon, A critical role for the right fronto-insular cortex in switching between central-executive and default-mode networks. *Proc Natl Acad Sci U S A* **105**, 12569 (2008).

91. W. T. Newsome, E. B. Pare, A selective impairment of motion perception following lesions of the middle temporal visual area (MT). *The Journal of neuroscience : the official journal of the Society for Neuroscience* **8(6)**, 2201 (1988).

92. R. Romo, A. Hernandez, A. Zainos, E. Salinas, Somatosensory discrimination based on cortical microstimulation. *Nature* **392**, 387 (1998).

93. J. R. Binder, E. Liebenthal, E. T. Possing, D. A. Medler, B. D. Ward, Neural correlates of sensory and decision processes in auditory object identification. *Nature neuroscience* **7**, 295 (2004).

94. K. H. Britten, M. N. Shadlen, W. T. Newsome, J. A. Movshon, The analysis of visual motion: A comparison of neuronal and psychophysical performance. *The Journal of neuroscience : the official journal of the Society for Neuroscience* **12**, 4745 (1992).

95. H. R. Heekeren, S. Marrett, D. A. Ruff, P. A. Bandettini, L. G. Ungerleider, Involvement of human left dorsolateral prefrontal cortex in perceptual decision making is independent of response modality. *Proceedings of the National Academy of Sciences of the United States of America* **103**, 10023 (2006).

96. A. D. Engell, G. McCarthy, Selective attention modulates face-specific induced gamma oscillations recorded from ventral occipitotemporal cortex. *The Journal of neuroscience : the official journal of the Society for Neuroscience* **30**, 8780 (2010).

97. G. Avidan, M. Behrmann, Functional MRI reveals compromised neural integrity of the face processing network in congenital prosopagnosia. *Current biology : CB* **19**, 1146 (2009).

98. J. V. Haxby *et al.*, Distributed and overlaping representations of faces and objects in ventral temporal cortex. *Science* **293**, 2425 (2001).

99. A. Ishai, Let's face it: it's a cortical network. *NeuroImage* **40**, 415 (2008).

100. V. T. Nguyen, M. Breakspear, R. Cunnington, Fusing concurrent EEG-fMRI with dynamic causal modeling: application to effective connectivity during face perception. *NeuroImage* **102 Pt 1**, 60 (2014).

101. N. Kanwisher, J. McDermott, M. M. Chun, The fusiform face area: A module in human extrastriate cortex specialized for face perception. *The Journal of neuroscience : the official journal of the Society for Neuroscience* **17(11)**, 4302 (1997).

102. N. Kanwisher, G. Yovel, The fusiform face area: a cortical region specialized for the perception of faces. *Philosophical transactions of the Royal Society of London. Series B, Biological sciences* **361**, 2109 (2006).

103. G. K. Aguirre, E. Zarahn, M. D'Esposito, An area within human ventral cortex sensitive to "building" stimuli: evidence and implications. *Neuron* **21**, 373 (1998).

104. R. Epstein, N. Kanwisher, A cortical representation of the local visual environment. *Nature* **392**, 598 (1998).

105. D. Baldauf, R. Desimone, Neural Mechanisms of object-based attention *Science* **344**, 424 (2014).

106. J. D. E. Gabrieli, R. A. Poldrack, J. E. Desmond, The role of left prefrontal cortex in language and memory. *Proc Natl Acad Sci USA* **95**, 906 (1998).

107. T. Carlson, M. J. Grol, F. A. Verstraten, Dynamics of visual recognition revealed by fMRI. *NeuroImage* **32**, 892 (2006).

108. M. Bar *et al.*, Cortical mechanisms specific to explicit visual object recognition. *Neuron* **29**, 529 (2001).

109. A. Pasupathy, E. K. Miller, Different time courses of learning-related activity in the prefrontal cortex and striatum. *Nature* **433**, 873 (2005).

110. N. U. Dosenbach *et al.*, A core system for the implementation of task sets. *Neuron* **50**, 799 (2006).

111. N. Medford, H. D. Critchley, Conjoint activity of anterior insular and anterior cingulate cortex: awareness and response. *Brain structure & function* **214**, 535 (2010).

112. V. Bonnelle *et al.*, Salience network integrity predicts default mode network function after traumatic brain injury. *Proceedings of the National Academy of Sciences of the United States of America* **109**, 4690 (2012).

113. S. Debener *et al.*, Trial-by-trial coupling of concurrent electroencephalogram and functional magnetic resonance imaging identifies the dynamics of performance monitoring. *The Journal of neuroscience : the official journal of the Society for Neuroscience* **25**, 11730 (2005).

114. R. Kiani, H. Esteky, K. Mirpour, K. Tanaka, Object category structure in response patterns of neuronal population in monkey inferior temporal cortex. *Journal of neurophysiology* **97**, 4296 (2007).

115. S. Li, S. D. Mayhew, Z. Kourtzi, Learning shapes the representation of behavioral choice in the human brain. *Neuron* **62**, 441 (2009).

116. B. Rossion *et al.*, A network of occipito-temporal face-sensitive areas besides the right middle fusiform gyrus is necessary for normal face processing. *Brain.* **126**, 2381 (2003).

117. B. Sorger, R. Goebel, C. Schiltz, B. Rossion, Understanding the functional neuroanatomy of acquired prosopagnosia. *NeuroImage* **35**, 836 (2007).

118. M. G. Philiastides, P. Sajda, EEG-informed fMRI reveals spatiotemporal characteristics of perceptual decision making. *The Journal of neuroscience : the official journal of the Society for Neuroscience* **27**, 13082 (2007).

119. J. Liu *et al.*, Neural Correlates of Covert Face Processing: fMRI Evidence from a Prosopagnosic Patient. *Cereb Cortex*, (2013).

120. B. M. Adhikari, K. Sathian, C. M. Epstein, B. Lamichhane, M. Dhamala, Oscillatory activity in neocortical networks during tactile discrimination near the limit of spatial acuity. *NeuroImage* **91**, 300 (2014).

121. C. H. Donahue, D. Lee, Dynamic routing of task-relevant signals for decision making in dorsolateral prefrontal cortex. *Nature neuroscience* **18**, 295 (2015).

122. M. J. Herrmann, A. C. Ehlis, A. Muehlberfer, A. J. Fallgatter, Source localization of early stages of face processing. *Brain Topography* **18**, 77 (2005).

123. J. K. Wynn, J. Lee, W. P. Horan, M. F. Green, Using event related potentials to explore stages of facial affect recognition deficits in schizophrenia. *Schizophrenia bulletin* **34**, 679 (2008).

124. P. Ekman, W. V. Friesen, Pictures of facial affect. *Palo Alto (CA): Consulting Psychologists Press*, (1976).

125. G. Rainer, E. K. Miller, Effects of visual experience on the representation of objects in the prefrontal cortex. *Neuron* **27**, 179 (2000).

126. M. Junghofer, T. Elbert, D. M. Tucker, B. Rockstroh, Statistical control of artifacts in dense array EEG/MEG studies. *Psychophysiol* **37**, 523 (2000).

127. R. D. Pascual-Marqui, C. M. Michel, D. Lehmann, Low resolution electromagnetic tomography: A new method for localizing electrical activity in the brain. *International journal of psychophysiology : official journal of the International Organization of Psychophysiology*, 49 (1994).

128. B. Clemens *et al.*, Theta EEG source localization using LORETA in partial epilepsy patients with and without medication. *Clinical neurophysiology : official journal of the International Federation of Clinical Neurophysiology* **121**, 848 (2010).

129. R. W. Thatcher, D. M. North, C. J. Biver, LORETA EEG phase reset of the default mode network. *Frontiers in human neuroscience* **8**, 529 (2014).

130. R. Jones, J. Bhattacharya, Alpha activity in the insula accompanies the urge to neutralize in sub-clinical obsessive-compulsive participants. *Journal of behavioral addictions* **1**, 96 (2012).

131. R. D. Pascual-Marqui *et al.*, Low resolution brain electromagnetic tomography (LORETA) functional imaging in acute, neuroleptic-naive, first-episode, productive schizophrenia. *Psychiatry Research Neuroimaging* **90**, 169 (1999).

132. C. M. Michel *et al.*, EEG source imaging. *Clinical neurophysiology : official journal of the International Federation of Clinical Neurophysiology* **115**, 2195 (2004).

133. A. Painold *et al.*, EEG low-resolution brain electromagnetic tomography (LORETA) in Huntington's disease. *Journal of neurology* **258**, 840 (2011).

134. R. D. Pascual-Marqui, C. M. Michel, D. Lehmann, Low resolution electromagnetic tomography: A new method for localizing electrical activity in the brain. *Int J Psychophysiol*, 49 (1994).

135. I. Haalman, E. Vaadia, Dynamics of neuronal interactions: relation to behavior, firing rates, and distance between neurons. *Human Brain Mapping* **5**, 249 (1997).

136. A. M. Dale, M. I. Sereno, Improved localization of cortical activity by combining EEG and MEG with MRI cortical surface reconstruction: A linear approach. *J Cogn Neurosci* **5**, 162 (1993).

137. M. Hamalainen, R. Hari, R. J. Ilmoniemi, J. Knuutila, O. V. Lounasmaa, Magnetoencephalography- theory, instrumentation, and applications to noninvasive studies of the working human brain. *Rev. Mod. Phys.* **65**, 413 (1993).

138. J. Cui, L. Xu, S. L. Bressler, M. Ding, H. Liang, BSMART: a Matlab/C toolbox for analysis of multichannel neural time series. *Neural networks : the official journal of the International Neural Network Society* **21**, 1094 (2008).

139. M. Ding, S. L. Bressler, W. Yang, H. Liang, Short-window spectral analysis of cortical event-related potentials by adaptive multivariate autoregressive modeling: data

preprocessing, model validation, and variability assessment. *Biological Cybernetics* **83**, 35 (2000).

140. R. C. Blair, W. Karniski, An alternative method for significance testing of waveform difference potentials. *Psychophysiol* **30**, 518 (1993).

141. D. J. Sheskin, Handbook of parametric and nonparametric statistical procedures. *Chapman & Hall/CRC Press* **Third Edition**, (2003).

142. Y. Benjamini, Y. Hochberg, Controlling the false discovery rate: A practical and powerful approach to multiple testing. *J Royal Statistical Society B (Methodological)*, 289 (1995).

143. B. R. Buchsbaum, S. Greer, W. L. Chang, K. F. Berman, Meta-analysis of neuroimaging studies of the Wisconsin card-sorting task and component processes. *Human brain mapping* **25**, 35 (2005).

144. L. J. Chang, T. Yarkoni, M. W. Khaw, A. G. Sanfey, Decoding the role of the insula in human cognition: functional parcellation and large-scale reverse inference. *Cerebral cortex* **23**, 739 (2013).

145. S. M. Nelson *et al.*, Role of the anterior insula in task-level control and focal attention. *Brain structure & function* **214**, 669 (2010).

146. T. Yarkoni, R. A. Poldrack, T. E. Nichols, D. C. Van Essen, T. D. Wager, Large-scale automated synthesis of human functional neuroimaging data. *Nature methods* **8**, 665 (2011).

147. B. Deen, N. B. Pitskel, K. A. Pelphrey, Three systems of insular functional connectivity identified with cluster analysis. *Cerebral cortex* **21**, 1498 (2011).

148. F. Cauda *et al.*, Functional connectivity of the insula in the resting brain. *NeuroImage* **55**, 8 (2011).

149. D. Swick, V. Ashley, U. Turken, Are the neural correlates of stopping and not going identical? Quantitative meta-analysis of two response inhibition tasks. *NeuroImage* **56**, 1655 (2011).

150. M. Ullsperger, H. A. Harsay, J. R. Wessel, K. R. Ridderinkhof, Conscious perception of errors and its relation to the anterior insula. *Brain Struct Funct* **214**, 629 (2010).

151. S. Dehaene, M. I. Posner, D. M. Tucker, Localization of a neural system for error-detection and compensation. *Psychol Sci* **5**, 303 (1994).

152. A. D. Craig, K. Chen, D. Bandy, E. M. Reiman, Thermosensory activation of insular cortex. *Nature neuroscience* **33**, 184 (2000).

153. R. Remedios, N. K. Logothetis, C. Kayser, An auditory region in the primate insular cortex responding preferentially to vocal communication sounds. *The Journal of neuroscience : the official journal of the Society for Neuroscience* **29**, 1034 (2009).

154. P. L. Smith, R. Ratcliff, Psychology and neurobiology of simple decisions. *Trends Neurosci* **27**, 161 (2004).

155. M. E. Mazurek, J. D. Roitman, J. Diterich, M. N. Shadlen, A role for neural integrators in perceptual decision making. *Cereb Cortex* **13**, 1257 (2003).

156. J. S. Ide, P. Shenoy, A. J. Yu, C. S. Li, Bayesian prediction and evaluation in the anterior cingulate cortex. *The Journal of neuroscience : the official journal of the Society for Neuroscience* **33**, 2039 (2013).

157. M. F. Rushworth, Intention, choice, and the medial frontal cortex. *Annals of the New York Academy of Sciences* **1124**, 181 (2008).

158. J. L. Vincent, I. Kahn, A. Z. Snyder, M. E. Raichle, R. L. Buckner, Evidence for a frontoparietal control system revealed by intrinsic functional connectivity. *J Neurophysiol* **100**, 3328 (2008).

159. M. P. van den Heuvel, R. C. Mandl, R. S. Kahn, H. E. Hulshoff Pol, Functionally linked resting-state networks reflect the underlying structural connectivity architecture of the human brain. *Human brain mapping* **30**, 3127 (2009).

160. L. Q. Uddin *et al.*, Dissociable connectivity within human angular gyrus and intraparietal sulcus: evidence from functional and structural connectivity. *Cereb Cortex* **20**, 2636 (2010).

161. A. Kucyi, M. Moayedi, I. Weissman-Fogel, M. Hodaie, K. D. Davis, Hemispheric asymmetry in white matter connectivity of the temporoparietal junction with the insula and prefrontal cortex. *PloS one* **7**, e35589 (2012).

162. M. Corbetta, G. Patel, G. L. Shulman, The reorienting system of the human brain: from environment to theory of mind. *Neuron* **58**, 306 (2008).

163. L. Q. Uddin, V. Menon, The anterior insula in autism: under-connected and under-examined. *Neurosci Biobehav Rev* **33**, 1198 (2009).

164. T. Singer, H. D. Critchley, K. Preuschoff, A common role of insula in feelings, empathy and uncertainty. *Trends in cognitive sciences* **13**, 334 (2009).

165. H. D. Critchley, J. Eccles, S. N. Garfinkel, Interaction between cognition, emotion, and the autonomic nervous system. *Handbook of Clinical Neurology* **117**, 59 (2013).

166. J. M. Allman *et al.*, The von Economo neurons in frontoinsular and anterior cingulate cortex in great apes and humans. *Brain structure & function* **214**, 495 (2010).

167. J. M. Allman, K. K. Watson, N. A. Tetreault, A. Y. Hakeem, Intuition and autism: a possible role for Von Economo neurons. *Trends in cognitive sciences* **9**, 367 (2005).

168. K. K. Watson, T. K. Jones, J. M. Allman, Dendritic architecture of the von Economo neurons. *Neuroscience* **141**, 1107 (2006).

169. J. M. Allman *et al.*, The von Economo neurons in the frontoinsular and anterior cingulate cortex. *Annals of the New York Academy of Sciences* **1225**, 59 (2011).

170. X. J. Wang, Decision making in recurrent neuronal circuits. *Neuron* **60**, 215 (2008).

171. D. J. Felleman, D. C. Van Essen, Distributed hierarchial processing in the primate cerebral cortex. *Cereb Cortex* **1**, 1 (1991).

172. M. Siegel, T. H. Donner, A. K. Engel, Spectral fingerprints of large-scale neuronal interactions. *Nature reviews. Neuroscience* **13**, 121 (2012).

173. S. Vanni, T. Tanskanen, M. Seppa, K. Uutela, R. Hari, Coinciding early activation of the human primary visual cortex and anteromedial cuneus. *Proceedings of the National Academy of Sciences of the United States of America* **98**, 2776 (2001).

174. A. Ishai, C. F. Schmidt, P. Boesiger, Face perception is mediated by a distributed cortical network. *Brain research bulletin* **67**, 87 (2005).

175. E. K. Miller, J. D. Cohen, An integrative theory of pretrontal cortex function. *Annu. Rev. Neurosci.* **24**, 167 (2001).

176. M. Petrides, D. N. Pandya, Dorsolateral prefrontal cortex: comparative cytoarchitectonic analysis in the human and the macaque brain and corticocortical connection patterns. *Eur. J. Neurosci.* **11**, 1011 (1999).

177. M.-T. Lu, J. B. Preston, P. L. Strick, Interconnections between the prefrontal cortex and the premotor areas in the frontal lobe. *J Com Neurol* **341**, 375 (1994).

178. P. J. Uhlhaas, W. Singer, Neural synchrony in brain disorders: relevance for cognitive dysfunctions and pathophysiology. *Neuron* **52**, 155 (2006).

179. G. B. Chand, M. Dhamala, Interactions among the default-mode, salience and central-executive networks during perceptual decision-making of moving dots. *Brain Connectivity (Revision)*, (2015).

180. N. Goulden *et al.*, The salience network is responsible for switching between the default mode network and the central executive network: Replication from DCM. *NeuroImage* **99**, 180 (2014).

APPENDIX

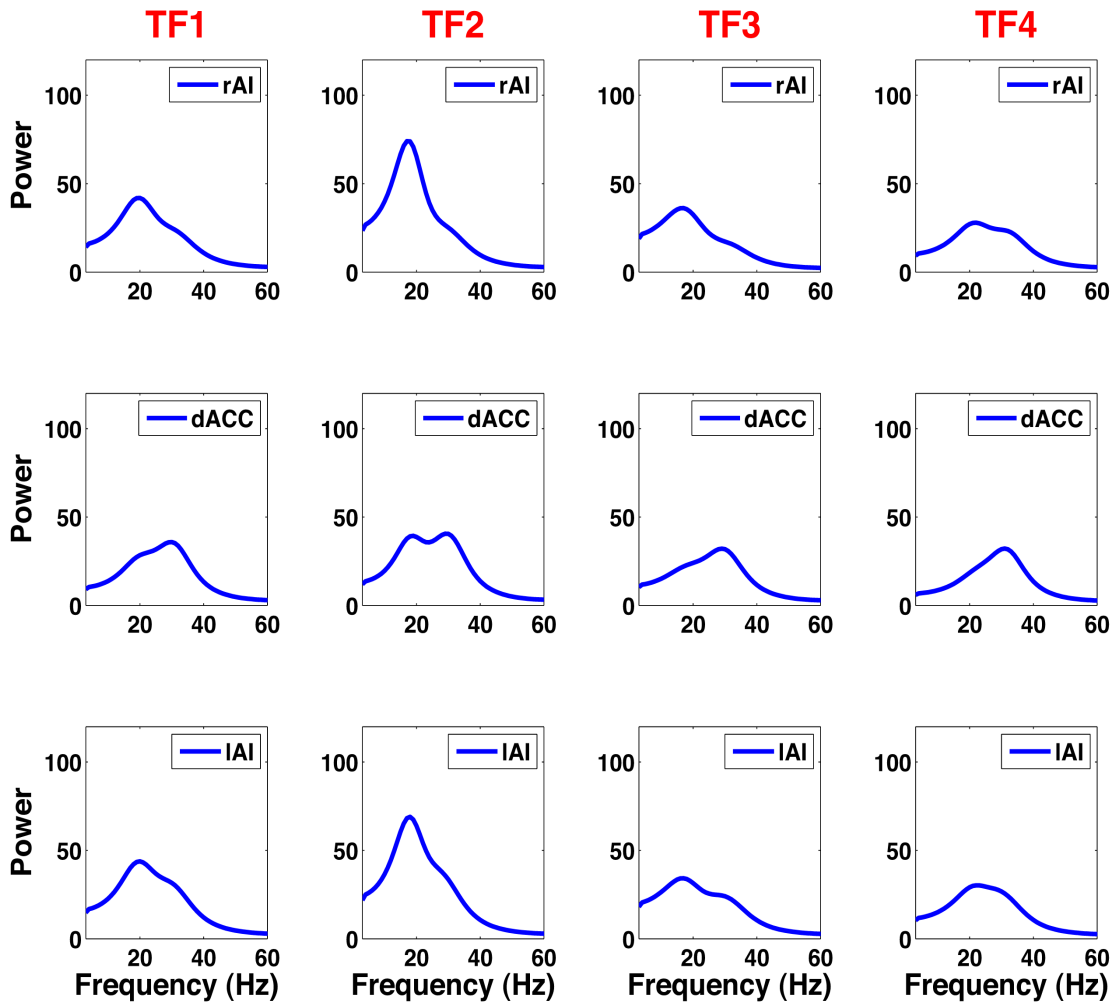

Figure A.1 Power spectra at the rAI (first row), dACC (second row), and lAI (third row) for stimuli with 0% noise-level at four consecutive time frames (TF1: 0 ms to 75 ms, TF2: 75 ms to 150 ms, TF3: 150 ms to 225 ms, and TF4: 225 ms to 300 ms) mentioned at the top of each column.

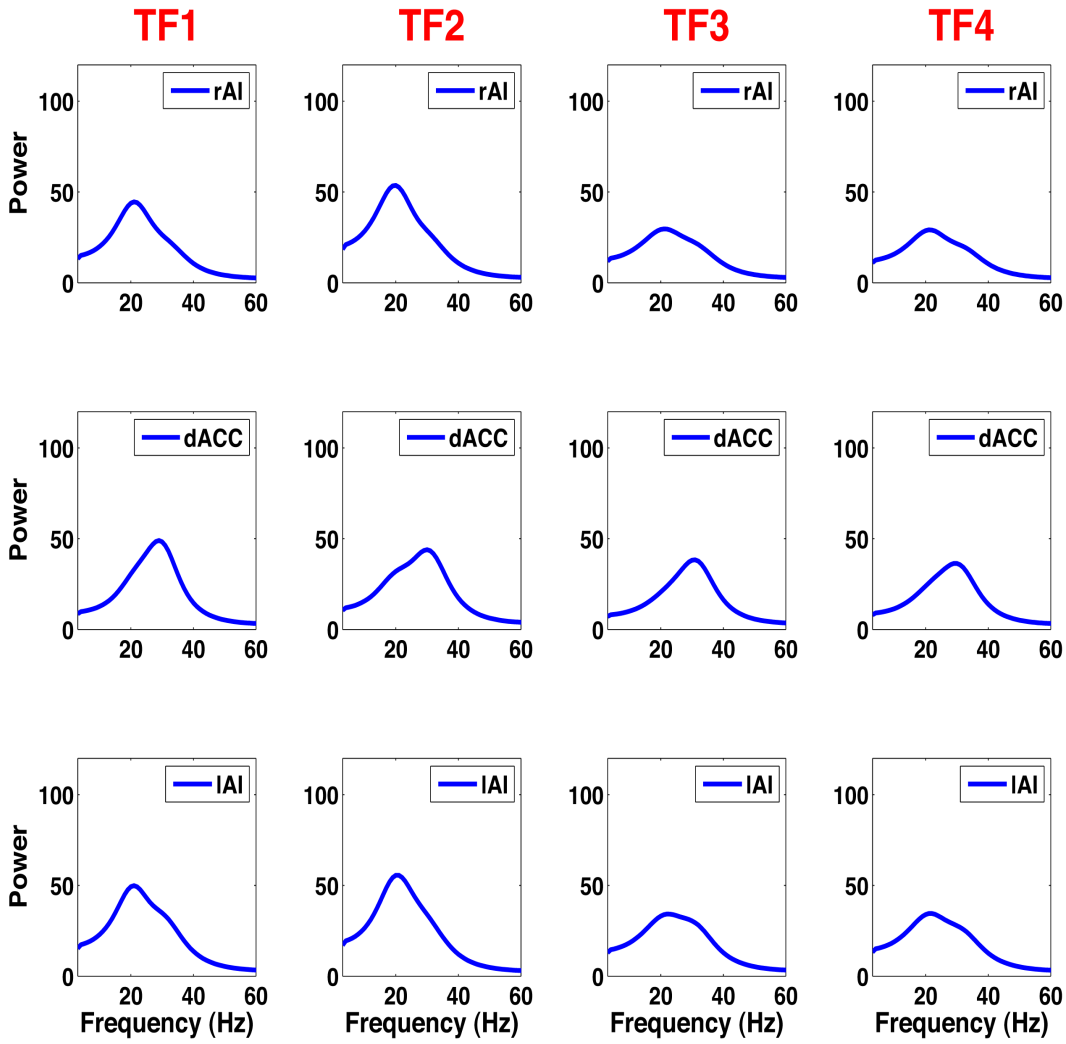

Figure A.2 Power spectra at the rAI (first row), dACC (second row), and lAI (third row) for stimuli with 40% noise-level at four consecutive time frames (TF1: 0 ms to 75 ms, TF2: 75 ms to 150 ms, TF3: 150 ms to 225 ms, and TF4: 225 ms to 300 ms) mentioned at the top of each column.

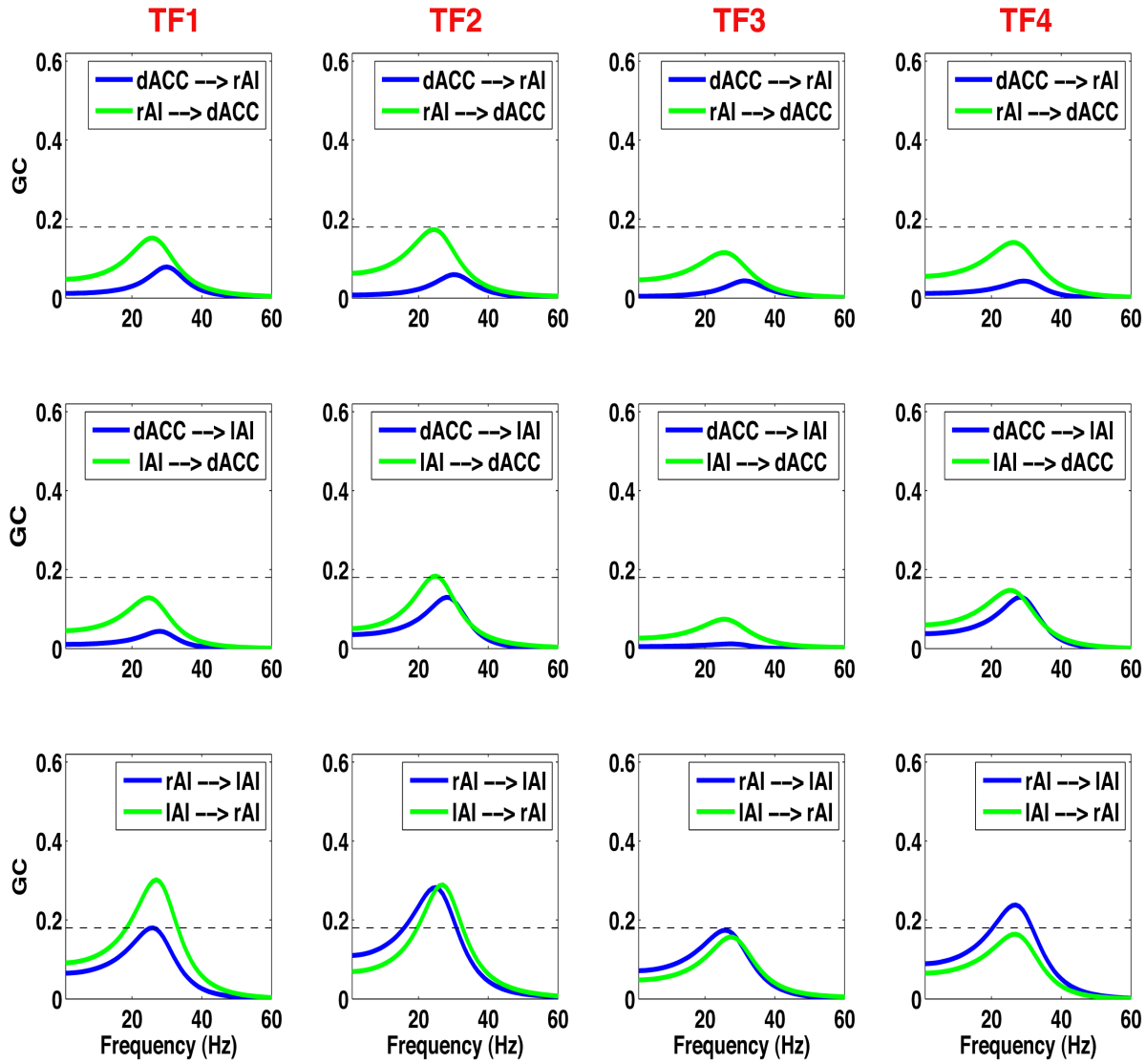

Figure A.3 Granger causality (GC) spectra of all possible pairs between the rAI, lAI, and dACC for stimuli with 40% noise-level at four consecutive time frames (TF1: 0 ms to 75 ms, TF2: 75 ms to 150 ms, TF3: 150 ms to 225 ms, and TF4: 225 ms to 300 ms) mentioned at top of each column.

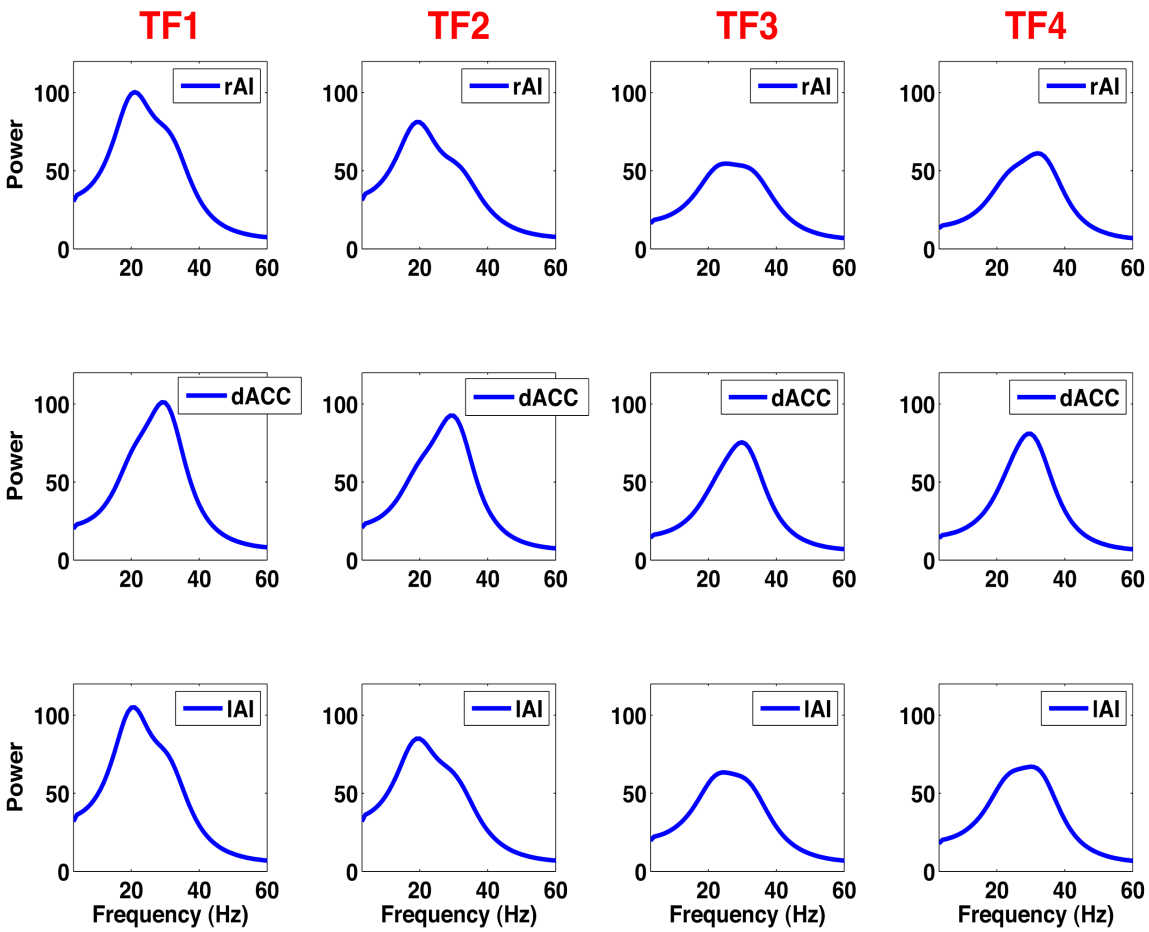

Figure A.4 Power spectra at the rAI (first row), dACC (second row), and lAI (third row) for stimuli with 55% noise-level at four consecutive time frames (TF1: 0 ms to 75 ms, TF2: 75 ms to 150 ms, TF3: 150 ms to 225 ms, and TF4: 225 ms to 300 ms) mentioned at the top of each column.

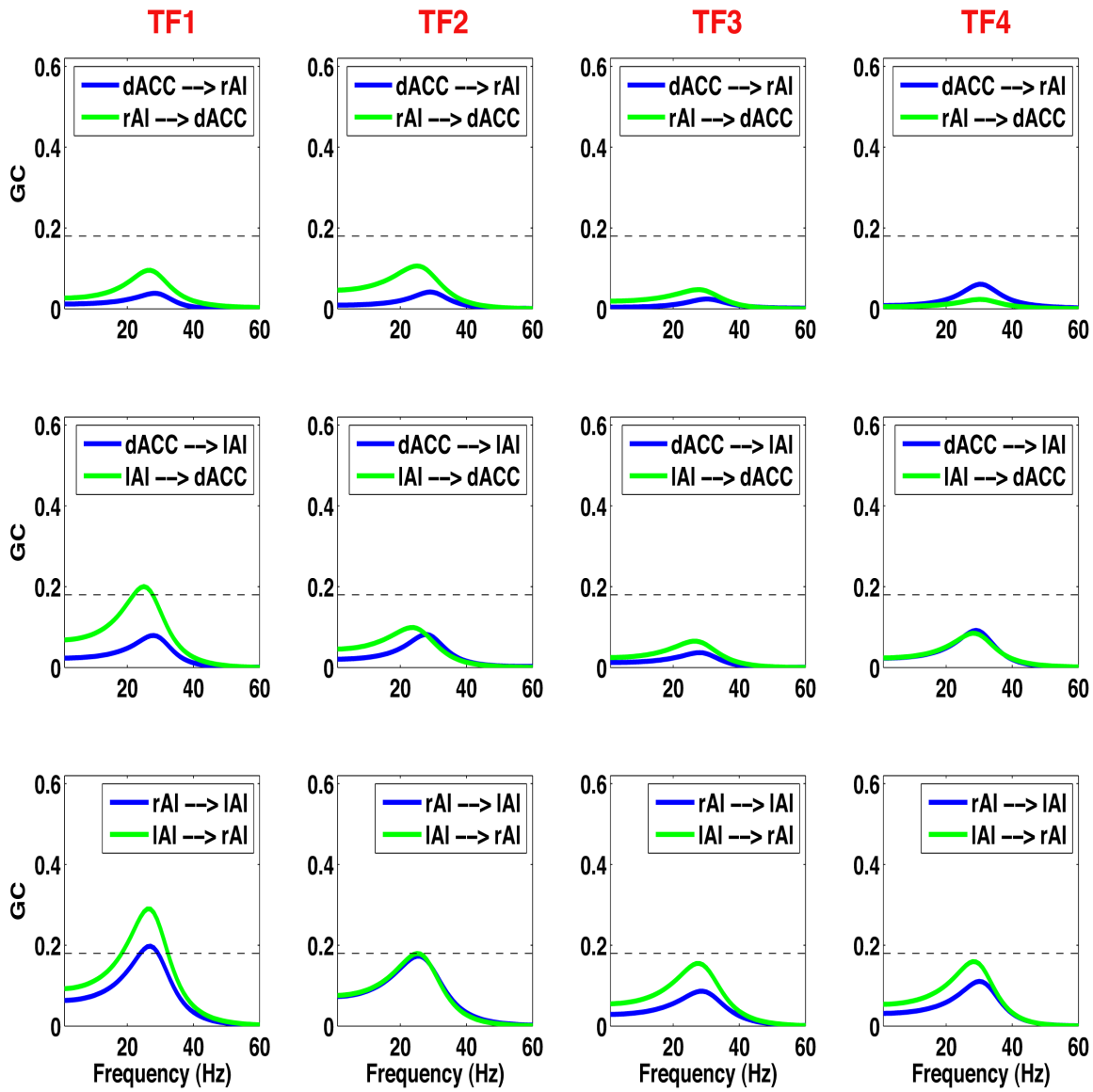

Figure A.5 Granger causality (GC) spectra of all possible pairs between the rAI, lAI, and dACC for stimuli with 55% noise-level at four consecutive time frames (TF1: 0 ms to 75 ms, TF2: 75 ms to 150 ms, TF3: 150 ms to 225 ms, and TF4: 225 ms to 300 ms) mentioned at top of each column.

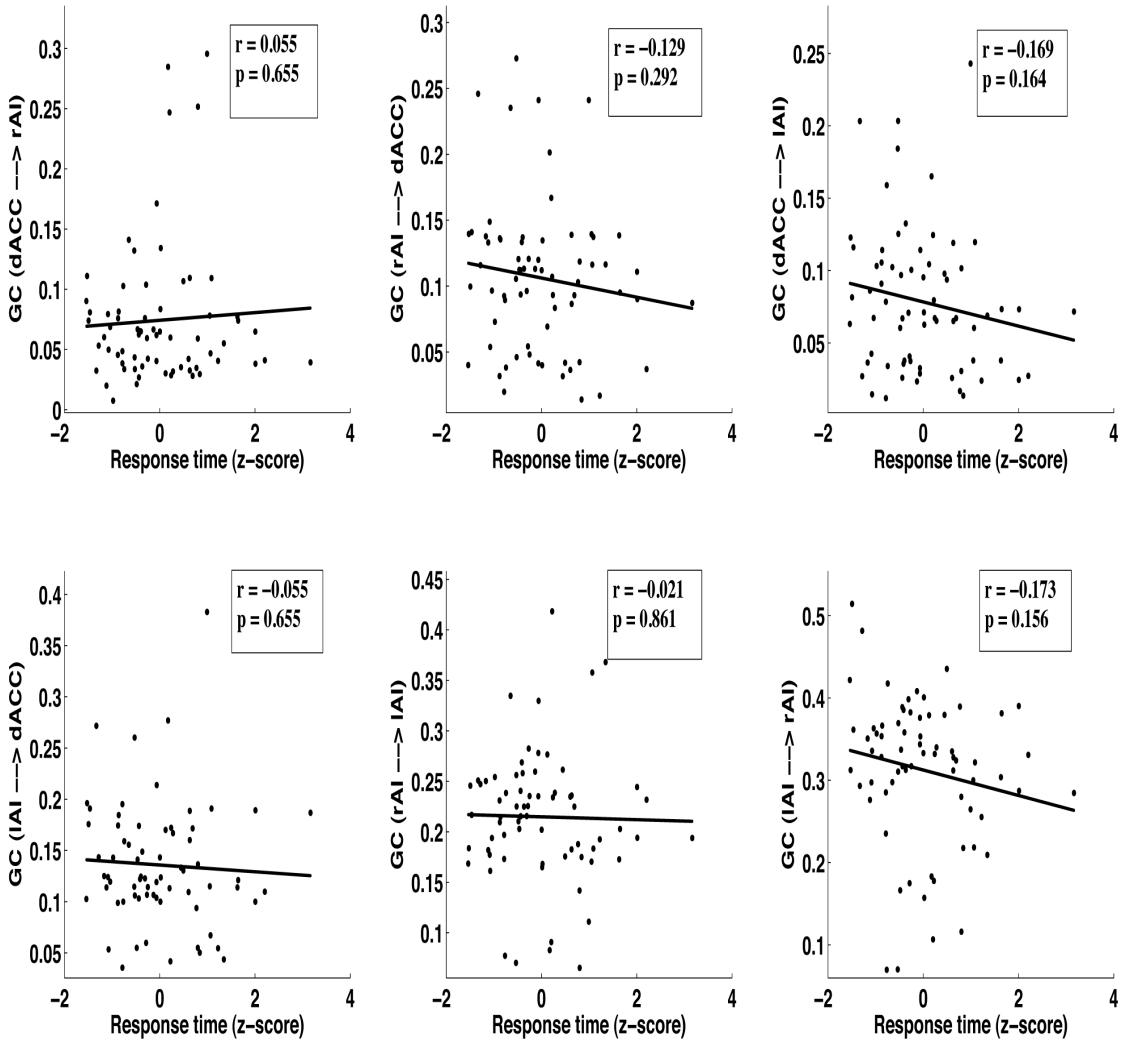

Figure A.6 Granger causality (GC) vs. difficulty level of tasks, expressed in terms of response time of all three noise-levels, in TF1: 75-150 ms (r represents correlation coefficient and $p < 0.05$ represents statistically significant correlation).

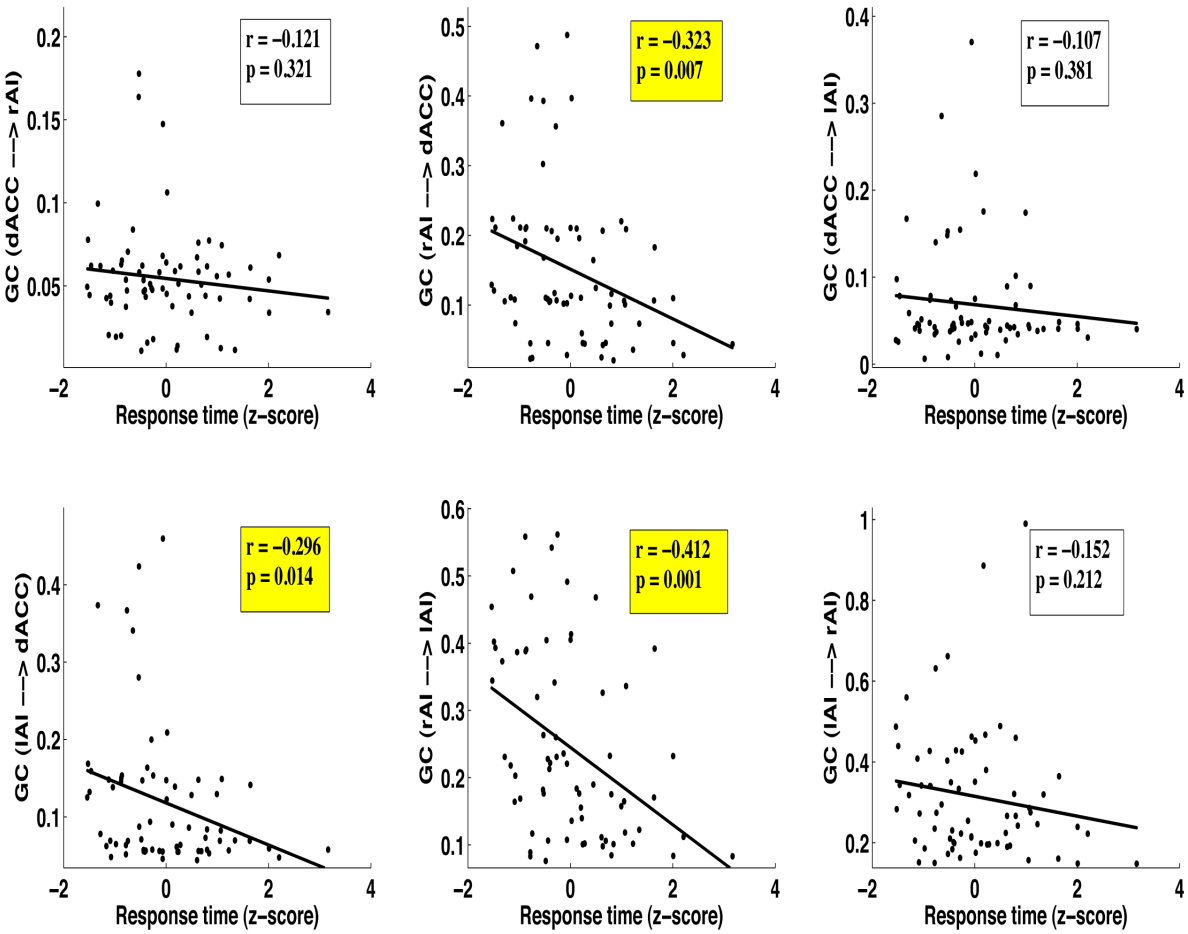

Figure A.7 Granger causality (GC) vs. difficulty level of tasks, expressed in terms of response time of all three noise-levels, in TF3: 150-225 ms (r represents correlation coefficient and $p < 0.05$ represents statistically significant correlation).

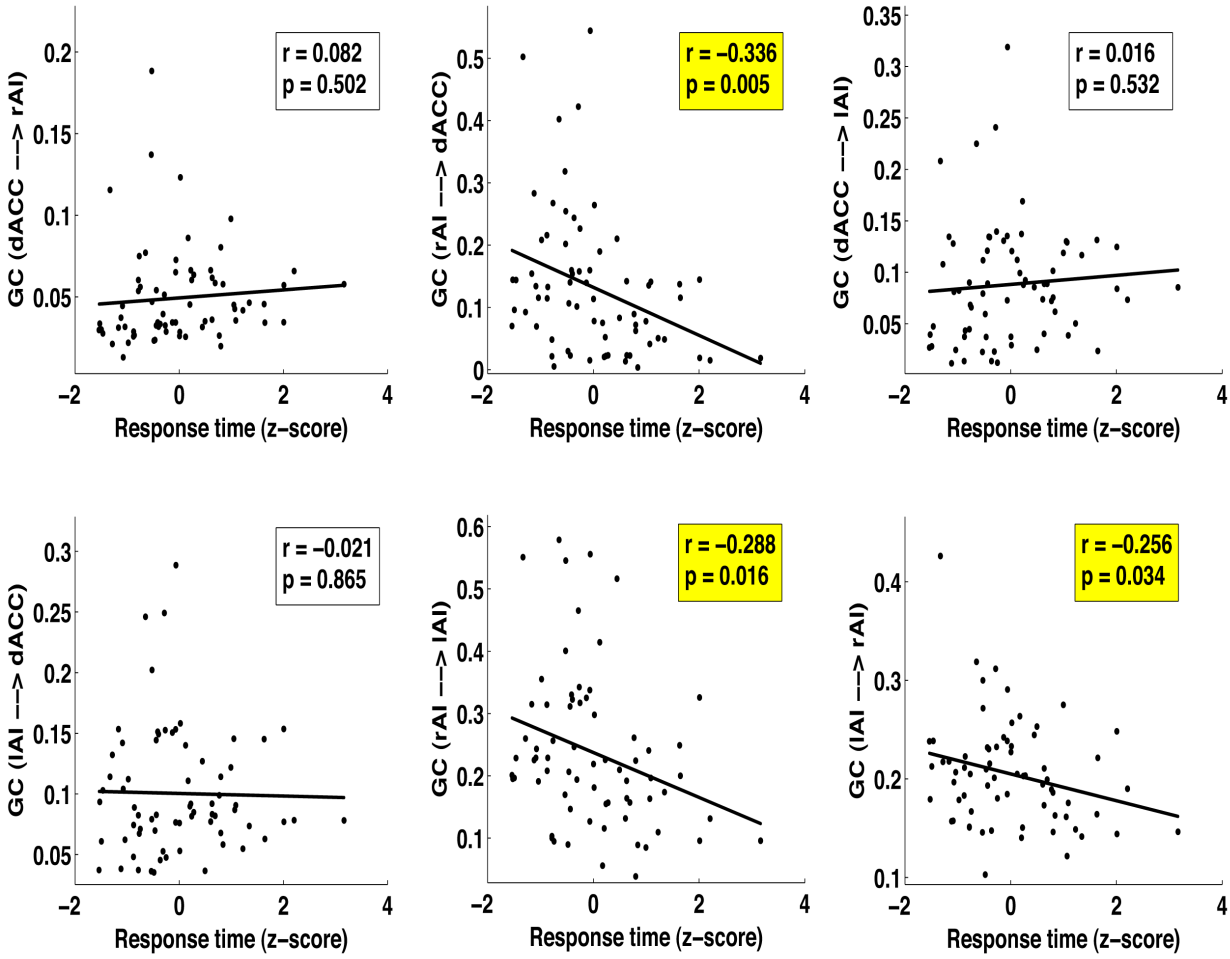

Figure A.8 Granger causality (GC) vs. difficulty level of tasks, expressed in terms of response time of all three noise-levels, in TF4: 225-300 ms (r represents correlation coefficient and $p < 0.05$ represents statistically significant correlation).